Nonlinear Model Inversion-Based Output Tracking Control for Battery Fast Charging

N.B. When citing this work, cite the original published paper.

(article starts on next page)

Nonlinear Model Inversion-Based Output Tracking Control for Battery Fast Charging

Yang Li, *Senior Member, IEEE,* Torsten Wik, *Member, IEEE,* Yicun Huang, and Changfu Zou, *Senior Member, IEEE*

Abstract—We propose a novel nonlinear control approach for fast charging of lithium-ion batteries, where health- and safety-related variables, or their time derivatives, are expressed in an input-polynomial form. By converting a constrained optimal control problem into an output tracking problem with multiple tracking references, the required control input, i.e., the charging current, is obtained by computing a series of candidate currents associated with different tracking references. Consequently, an optimization-free nonlinear model inversion-based control algorithm is derived for charging the batteries. We demonstrate the efficacy of our method using a spatially discretized high-fidelity pseudo-two-dimensional (P2D) model with thermal dynamics. Conventional methods require computationally demanding optimization to solve the corresponding fast charging problem for such a high-order system, leading to practical difficulties in achieving low-cost implementation. Results from comparative studies show that the proposed controller can achieve performance very close to nonlinear and linearized model predictive control but with much lower computational costs and minimal parameter tuning efforts.

Index Terms—Electrochemical-thermal model, fast charging, inversion-based control, lithium plating (LiP), lithium-ion batteries.

NOMENCLATURE

Symbol:

A	Cross-sectional area (m^2).
C_T	Battery thermal capacitance (J/K).
D_e, D_s	Electrolyte and solid-phase diffusion coefficients (m^2/s).
$\mathcal{D}$	Physical domain ($\mathcal{D} \in \{\text{pos}, \text{neg}, \text{sep}\}$).
$\mathcal{F}$	Faraday constant (96, 487 C/mol).
I_{app}	Applied charging current (A).
I_e, I_s	Electrolyte and solid-phase currents (A).
I_n	Current due to molar flux of intercalation (A).
M	Order of solid-phase reduced-order model.
N^{tot}	Total number of control volumes.
P_{bat}	Battery charging power (W).
$\mathcal{Q}_{\text{max}}$	Battery capacity (Ah).
Q_T	Heat generation (W).
$\mathcal{R}$	Universal gas constant [8.314 J/(K · mol)].
R_{col}	Current collector resistance (Ω).
R_{ct}	Charge-transfer resistance (Ω).
R_e, R_s	Electrolyte and solid-phase resistances (Ω).
R_f	Solid-electrolyte interphase film resistance (Ω).
R_T	Battery thermal resistance (K/W).
R_p	Particle radius (m).
SOC	State of charge.
T	Battery temperature (K).
T_{amb}	Ambient temperature (K).
T_{ref}	Reference temperature (298.15 K).
U_e	Electrolyte diffusion overpotential (V).
U_{ss}	Equilibrium potential of an electrode (V).
V_{bat}	Battery terminal voltage (V).
Φ_e, Φ_s	Electrolyte and solid-phase potentials (V).
a_s	Surface area per unit electrode volume (1/m).
c_e, c_s	Electrolyte and solid-phase concentrations (mol/m^3).
c_e^0	Average electrolyte concentration (mol/m^3).
$c_{s,\text{avg}}$	Volume-averaged concentration in the solid phase (mol/m^3).
$c_{s,\text{max}}$	Maximum concentration in the solid phase (mol/m^3).
c_{ss}	Surface concentration in the solid phase (mol/m^3).
$h^{[l]}$	State-dependent coefficient.
i_0	Exchange current density (A/m^2).
j_{SEI}	SEI side-reaction molar flux [mol/(m^2· s)].
j_n	Molar flux due to intercalation [mol/(m^2· s)].
k	Electrode reaction constant (A · m$^{2.5}$/mol$^{1.5}$).
$\Delta \delta$	Width of a control volume (m).
r_{ct}	Areal charge-transfer resistance ($\Omega \cdot$ m^2).
r_f	Areal film resistance ($\Omega \cdot$ m^2).
t_a^0	Transference number.
u, x, y	Input, state, output.
α, β	Coefficients of solid-phase reduced-order diffusion model.
η_{LiP}	Lithium plating potential (V).
η_{SEI}	SEI side-reaction potential (V).
$\varepsilon_e, \varepsilon_s$	Electrolyte and solid-phase volume fractions.
κ, σ	Electrolyte and solid-phase conductivities (S/m).
τ	Time constant (s).
Δt	Sampling time (s).

Subscript:

i	Control volume index. $i \in \{1, 2, \cdots, N^{\text{tot}}\}$.
$i \pm 0.5$	Variable at the edges of ith control volume. $i \in \{1, 2, \cdots, N^{\text{tot}}\}$.

j	Index of output tracking control mode.
m	Index of state in the solid-phase reduced-order model.
0%	Value at SOC = 0%.
100%	Value at SOC = 100%.
LiP	Lithium plating.
SEI	Solid-electrolyte interphase film.

Superscript:

eff	Effective.
pos	Positive electrode.
neg	Negative electrode.
sep	Separator.
sep/neg	Separator/negative electrode interface.
neg/col	Negative electrode/current collector interface.
ZIR	Zero-input response.
ZSR	Zero-state response.

I. INTRODUCTION

IN 2021, the median driving range of new conventional fossil-fueled vehicles is 648 km, while that of the latest Li-ion battery-powered electric vehicles (EVs) is only 376 km [1]. The resulting range anxiety experienced by EV drivers can be alleviated by regular fast battery recharging, especially for long-range excursions or emergency use. In contrast to conventional fossil-fueled vehicles, EVs suffer from the notorious issue of long charging time, which can cause long queues at the charging station and serious road congestion nearby as the penetration level of EVs increases. Conservative low-to-medium charging rates are often applied at present, including commercially-viable charging protocols such as constant-current constant-voltage (CC-CV), constant-power constant-voltage (CP-CV), CV-CC-CV [2], multistage CC (MCC) [3], and boost charging [4]. These model-free and heuristic methods are characterized by predefined profiles with constant current, voltage, and/or power, while the internal dynamics of the battery are completely ignored due to a lack of relevant information. Under this condition, simply increasing the charging current rates will unfavorably speed up the battery aging, cause damage, and even pose serious hazards to EV users [5].

The required internal information can be provided by various battery models, with which model-based charging strategies can be designed. Conventionally, lumped-parameter equivalent circuit models (ECMs) with simple circuit structures are used. State-of-charge (SOC), state-of-health, and internal temperature are used to design various charging strategies based on frequency optimization [6], multi-objective optimization, fuzzy control [7], and model predictive control (MPC) [8]. On the other hand, physics-based models (PBMs) have recently been investigated for the design of fast charging algorithms [9]. These mechanistic models describe internal electrochemical phenomena, such as ion diffusion, intercalation kinetics, and heat generation and transfer, and are capable of reproducing battery dynamics with high fidelity. More importantly, data-driven approaches, while receiving extensive research attention in recent years [10], [11], may

struggle to uncover the kinds of health and safety-related internal information that PBMs can provide. Based on PBMs, optimization problems and open-loop optimal controls have been formulated to minimize charging duration [12]. These results can be regarded as the first step toward the design of closed-loop controllers that are able to compensate for model uncertainties and disturbances.

Recently, several charging algorithms with closed-loop control algorithms have been proposed. For instance, a fast-charging strategy was developed by incorporating an isothermal electrochemical model and health-related constraints into a nonlinear MPC (NMPC) algorithm [13]. A one-step NMPC was proposed to optimize charging profiles by integrating thermal dynamics into a multi-physics pseudo-two-dimensional (P2D) model described by partial-differential-algebraic equations (PDAEs), [14]. However, the potential applications of these strategies may be limited by their computationally intensive nature, as they require handling nonlinear PDAEs and performing real-time nonlinear optimization.

Similarly, in [15], dynamic programming was utilized to obtain the global solution of the fast charging problem with the P2D model. However, due to the curse of dimensionality, the authors were forced to coarsely divide the time, resulting in a five-step MCC that significantly deviates from the optimal solution presented in [14]. To address the problem of low computational efficiency, a novel approach was proposed in [16] using a reduced-order model (ROM) of Li-ion battery and a linear time-varying MPC (LTV-MPC). However, this method has the limitation of ignoring the nonuniform effect over the electrode thickness, which may lead to inaccurate results in certain applications. The concept of using a ROM is also employed in the design of a reference governor for achieving a low-complexity fast charging strategy in [17] and further enhanced and experimentally validated in [18]. To develop the ROMs, most existing fast charging strategies make use of the assumption that the battery behaviors are uniform over each electrode. This allows for a significant reduction in both modeling and computational complexity [9]. Recent efforts have been directed at solving an optimization problem formulated with a high-order electrochemical-thermal-aging model using nonlinear programming [19]. The model considers an extended SPM, an enhanced two-state thermal model, and an SEI film growth model with solvent concentration evolution. The algorithm shows excellent offline performance for the optimization of the charging curves.

However, neglecting the nonuniformity in Li-ion battery electrodes can result in inaccurate prediction of battery degradation, particularly in the context of fast charging. For example, spatially uneven development of lithium plating and solid-electrolyte interphase (SEI) film is commonly observed, and under extremely high charging current conditions, this phenomenon can be significantly amplified due to certain chain effects [20]. The assumption of uniform electrode behavior can cause significant modeling errors and result in overly aggressive control algorithms, particularly for high-energy battery cells with thick electrodes [21]. A ROM based on frequency-response function and subspace-based identification can achieve high computational efficiency by selecting local

variables at critical spatial positions, but its effectiveness is limited to cases where only two constraints are considered [22]. The complexity and efficiency of this technique have not been demonstrated for more constraints and more physical dynamics such as concentrations, SEI film growth, heat generation and transfer.

To address the challenge of modeling nonuniformity in Li-ion battery electrodes, well-established spatial discretization methods, such as the finite volume method (FVM) [23] and spectral methods [24], [25] can be applied to simplify the multiphysics PDAE model, enabling accurate capture of spatially distributed dynamics. For example, in [23], the model is reformulated as a multiphysics distributed-parameter circuit network, overcoming the limitations of the existing *ad-hoc* ROMs. These high-dimensional models have been used to develop initial NMPC-based fast charging strategies, demonstrating their potential for future implementation [26].

Unfortunately, high-dimensional nonlinear systems pose fundamental difficulties for control algorithms that require online optimization, such as LTV-MPC and NMPC. Despite the ever-increasing computational capability for modern onboard controllers, alleviating computational burden remains desirable for practical and cost-effective implementation. In our previous work, we have shown that by considering the fact that the charging current is limited by different operating constraints, a physical-constraint-triggered proportional-integral (PCT-PI) controller can be designed without the need of computationally demanding online optimization [27]. The constraints are activated alternately and the PI controller's internal states are switched with bumpless transfer. The algorithm achieves comparable computational efficiency to a simple PI controller and a near-optimal charging profile compared to the NMPC with a short prediction horizon. However, for either NMPC or PI control, performance is significantly affected by control parameters. Due to the complexity of the model, it is difficult to adjust the control parameters according to an analytical method, so only a labor-extensive trial-and-error method can be used. The tuning of the control parameters has to be carried out individually for different batteries with different characteristics, and the parameters need to be re-tuned as the aging-affected parameters change over time. Inappropriately selected control parameters can cause system instability problems, and even under the optimal controller settings, some overshoots cannot be avoided.

To sidestep the computational problems in optimization-based methods and to simplify the parameter tuning in many feedback control strategies, in this work, we propose a nonlinear battery charging control method based on model inversion techniques. An electrochemical-thermal P2D model of the Li-ion batteries is used to demonstrate the design procedure. The novelty and contributions of this method are described as follows. First, we show that by applying the FVM on the electrode scale and reducing the model using a moment-matching method on the particle scale, many variables for control interest, or their first-order time derivatives, can be expressed as an input-affine or an input-quadratic form. This fact motivates us to derive analytical solutions to a series of output tracking problems so that the required input charging

current can be computed using the high-fidelity battery model. Consequently, the original constrained optimal control problem is converted to a multiple-output tracking problem that can be solved without optimization. By ensuring the charging current meets all constraints in the outputs, the proposed optimization-free nonlinear inversion-based output tracking control strategy requires almost ignorable parameter tuning efforts. It is shown that the proposed algorithm can achieve comparable numerical accuracy to MPC-based solutions but largely outperforms them in terms of computational efficiency. Due to the high computational efficiency, the proposed algorithm is also very useful for control-oriented identification of PBM parameters where massive simulations with closed-loop control are needed.

The rest of the paper is organized as follows. In Section II, we first present a spatially discretized representation of the P2D model and typical health- and safety-related constraints of fast charging. In Section III, a general fast charging control problem is formulated, and we describe the proposed nonlinear model inversion-based control approach for solving such a problem in Section IV. In Section V, we show that the discretized P2D model is suitable for the proposed inversion-based control and corresponding state-dependent coefficients are derived. Illustrative examples are given to examine the effectiveness of the proposed fast-charging method in Section VI, followed by the concluding remarks in Section VII.

II. ELECTROCHEMICAL-THERMAL OF MODEL AND CONSTRAINTS FOR BATTERY CHARGING

A. Physics-Based Modeling

A typical Li-ion battery features a sandwich-like structure that includes the positive electrode, the separator, the negative electrode, as well as the current collectors attached to the ends of the electrodes [28]. To reflect the multi-physics nature of the Li-ion battery during fast charging, a P2D model with thermal dynamics is considered the very precise mathematical description under wide regimes of applied current rates and temperatures, exhibiting many internal health- and safety-related behaviors [29]. More details of the P2D model can be founded in [9], [23], [30], [31]. To facilitate the charging algorithm development, the P2D model is spatially discretized using the FVM and can be explained with the aid of the equivalent circuit network in Fig. 1.

Notation: We use the superscripts $\mathcal{D} \in \{\text{pos}, \text{neg}, \text{sep}\}$ to indicate whether physical quantities are in the positive electrode, the negative electrode, or the separator domains, respectively. A subscript i is attached to indicate the local value in the ith control volume of a spatiotemporal quantity. The subscript $i + 0.5$ represents a component connecting two elements in the ith and the $(i + 1)$th control volumes. Furthermore, the following index sets are defined. $\mathcal{I}^{\text{pos}} := \{1, 2, \cdots, N^{\text{pos}}\}$, $\mathcal{I}^{\text{sep}} := \{N^{\text{pos}}+1, N^{\text{pos}}+2, \cdots, N^{\text{pos}}+N^{\text{sep}}\}$, $\mathcal{I}^{\text{neg}} := \{N^{\text{pos}}+N^{\text{sep}}+1, N^{\text{pos}}+N^{\text{sep}}+2, \cdots, N^{\text{pos}}+N^{\text{sep}}+N^{\text{neg}}\}$ where N represents the number of control volumes in the corresponding domain. We also denote $N^{\text{tot}} := N^{\text{pos}}+N^{\text{sep}}+N^{\text{neg}}$ as the total number of control volumes and $N^{\text{sep/neg}} := N^{\text{pos}} + N^{\text{sep}} + 1$ as the index of the control volume at the separator/negative
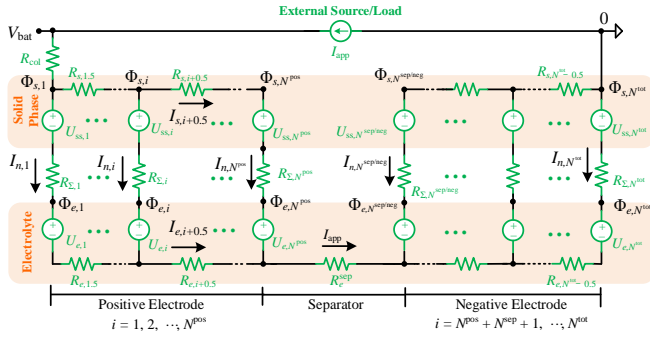
Fig. 1. Equivalent circuit network for Li-ion batteries. The voltage sources are controlled by battery temperature and concentrations, governed by heat and mass transfer equations, respectively.

electrode interface. Furthermore, $\mathcal{I}' := \{1, 2, \ldots, N^{\text{pos}} - 1\} \cup \{N^{\text{pos}} + N^{\text{sep}} + 1, \cdots, N^{\text{tot}} - 1\}$ is used to represent all currents or resistances on the horizontal branches (i.e., with an index $i + 0.5$) in the electrodes, as shown in Fig. 1. The width and cross-sectional area of the ith control volume are denoted by $\Delta\delta_i$ and A, respectively.

1) An Equivalent Circuit Network: The equivalent circuit network in Fig. 1 consists of elements including the input current source I_{app}, voltage sources ($U_{\text{ss},i}$ and $U_{e,i}$, $\forall i \in \mathcal{I}^{\text{pos}} \cup \mathcal{I}^{\text{neg}}$), and various resistors. The circuit represents the algebraic equations (AEs) in the P2D model. The voltage sources and resistances are not constant. As shown in Appendix A, these elements are functions of system states, i.e., solid-phase surface concentration ($c_{\text{ss},i}$), electrolyte concentrations ($c_{e,i}$), and battery temperature T, and thus they can be regarded as state-dependent variables. According to the circuit theory, given the input current, the voltage sources, and the resistances, one can solve the AEs for all the branch currents, i.e., the intercalation currents $I_{n,i}$, the electrolyte currents $I_{e,i+0.5}$, and the solid-phase currents $I_{s,i+0.5}$. The close-form solution to $I_{n,i}$ can be expressed in the form of [see eqs. (C.1) and (C.2) in [23]]

$$I_{n,i} = I_{n,i}^{\text{ZIR}}(x) + K_{n,i}^{\text{ZSR}}(x)I_{\text{app}} \quad \forall i \in \mathcal{I}^{\text{pos}} \cup \mathcal{I}^{\text{neg}}. \quad (1)$$

Similarly, $I_{e,i+0.5}$ and $I_{s,i+0.5}$ can be expressed as

$$I_{e,i+0.5} = I_{e,i+0.5}^{\text{ZIR}}(x) + K_{e,i+0.5}^{\text{ZSR}}(x)I_{\text{app}} \quad \forall i \in \mathcal{I}', \quad (2)$$

$$I_{s,i+0.5} = I_{s,i+0.5}^{\text{ZIR}}(x) + K_{s,i+0.5}^{\text{ZSR}}(x)I_{\text{app}} \quad \forall i \in \mathcal{I}'. \quad (3)$$

Here, each solution in (1)–(3) consists of a zero-input-response (ZIR) component and a zero-state-response (ZSR) component. The ZIR component I^{ZIR} is the solution when the input current is zero ($u = I_{\text{app}} = 0$), and thus it has only dependency on the model state x but is not directly affected by the input u. On the other hand, the ZSR component is the solution when the voltage sources are all zero, and it has a linear relationship with the input current while the gain K^{ZSR} is state-dependent.

The battery voltage and power can then be calculated by

$$\begin{aligned} V_{\text{bat}} =&(U_{\text{ss},i} + U_{e,i} + R_{\Sigma,i}I_{n,i})|_{i=1} - \\ &(U_{\text{ss},i} + U_{e,i} + R_{\Sigma,i}I_{n,i})|_{i=N^{\text{tot}}} + \\ &\sum_{i \in \mathcal{I}'}(R_{e,i+0.5}I_{e,i+0.5}) + R_e^{\text{sep}}I_{\text{app}} + R_{\text{col}}I_{\text{app}}, \quad (4) \end{aligned}$$

$$P_{\text{bat}} = V_{\text{bat}}I_{\text{app}}. \quad (5)$$

For health-aware charging control, we are particularly interested in the side reaction potential of lithium plating (LiP) (namely, the anode potential, as used in many existing works):

$$\eta_{\text{LiP},i} = \Phi_{s,i} - \Phi_{e,i} = U_{\text{ss},i} + R_{\Sigma,i}I_{n,i}. \quad (6)$$

The second side reaction is regarding the SEI, and its governing equations are

$$\begin{aligned} \eta_{\text{SEI},i} &= \Phi_{s,i} - \Phi_{e,i} - U_{\text{SEI}} - R_{f,i}I_{n,i} \\ &= U_{\text{ss},i} + R_{\text{ct},i}I_{n,i} - U_{\text{SEI}}. \quad (7) \end{aligned}$$

$$j_{\text{SEI},i} = -\frac{i_{0,\text{SEI}}}{\mathcal{F}} \exp\left(-\frac{\mathcal{F}}{2\mathcal{R}T}\eta_{\text{SEI},i}\right) \quad (8)$$

where η_{SEI} is the SEI side-reaction overpotential, $j_{\text{SEI},i}$ is the molar flux of the SEI side reactions, $i_{0,\text{SEI}}$ is the side-reaction exchange current density, U_{SEI} is the side reaction equilibrium potential. Furthermore, $\mathcal{R}$, $\mathcal{F}$, and T are the universal gas constant, the Faraday constant, and battery temperature, respectively.

2) Update of Solid-Phase Concentration States: The dynamics of the battery are governed by a set of ODEs, describing the evolution of the concentrations and temperature over time. These ODEs are used to update the system's state and then the voltage sources and resistances of the circuit in Fig. 1. The ODEs governing the concentrations can be obtained by reducing the original PDE-based solid-phase diffusion equations with various model reduction methods [9]. We apply a frequency-domain method proposed in [32] to obtain a reduced-order diffusion submodel:

$$\dot{\tilde{c}}_{s,i,m} = -\frac{\alpha_m D_{s,i}^{\text{eff}}}{R_{p,i}^2}\tilde{c}_{s,i,m} - \frac{\beta_m}{R_{p,i}}\frac{I_{n,i}}{\mathcal{F}A\Delta\delta_i a_{s,i}}, \quad (9)$$

$$c_{\text{ss},i} = \sum_{m=1}^{M}\tilde{c}_{s,i,m}, \quad (10)$$

$$c_{s,\text{avg},i} = \tilde{c}_{s,i,1}, \quad (11)$$

$\forall i \in \mathcal{I}^{\text{pos}} \cup \mathcal{I}^{\text{neg}}, \forall m \in \{1, 2, \cdots, M\}$. $c_{s,\text{avg},i}$ is the volume-averaged solid-phase concentration, $R_{p,i}$ is the particle radius, and $D_{s,i}^{\text{eff}}$ is the effective solid-phase diffusion coefficient, $a_{s,i}$ is the specific electrode area, and α_m and β_m are dimensionless coefficients.

The SOC of the battery can be determined by considering the bulk concentration, $c_{s,\text{avg},i}$, in either the negative electrode [14], [26] or the positive one [19]. The former is more convenient since the bulk concentration in the negative electrode is positively correlated to battery SOC. In the present model, the SOC is expressed by

$$\text{SOC} = \frac{\frac{1}{\delta^{\text{neg}}}\sum_{i \in \mathcal{I}^{\text{neg}}}(\Delta\delta_i c_{s,\text{avg},i}) - c_{s,0\%}^{\text{neg}}}{c_{s,100\%}^{\text{neg}} - c_{s,0\%}^{\text{neg}}}, \quad (12)$$

where δ^{neg} is the thickness of the negative electrode. $c_{s,0\%}^{\text{neg}}$ and $c_{s,100\%}^{\text{neg}}$ are concentrations when the battery is considered to be fully discharged and charged, respectively. It is worth noting that in practical scenarios, the capacity of the battery is typically constrained by the capacity of the positive electrode. This is because the negative electrode is often designed with a

higher capacity to account for its faster degradation over time [33].

3) Update of Electrolyte Concentration States: The electrolyte concentration $c_{e,i}$ is solved via the FVM:

$$\dot{c}_{e,i} = \frac{1}{\Delta\delta_i \varepsilon_{e,i}} \left(\frac{D_{e,i+0.5}^{\text{eff}}}{0.5} \frac{c_{e,i+1} - c_{e,i}}{\Delta\delta_{i+1} + \Delta\delta_i} \right.$$
$$\left. - \frac{D_{e,i-0.5}^{\text{eff}}}{0.5} \frac{c_{e,i} - c_{e,i-1}}{\Delta\delta_{i-1} + \Delta\delta_i} \right) + \lambda_i, \quad (13)$$

with $c_{e,i} = c_{e,i-1}$ for $i = 1$, $c_{e,i+1} = c_{e,i}$ for $i = N^{\text{tot}}$, and

$$\lambda_i = \begin{cases} \frac{t_a^0}{\varepsilon_{e,i}} \frac{I_{n,i}}{\mathcal{F} A \Delta\delta_i}, & i \in \mathcal{I}^{\text{pos}} \cup \mathcal{I}^{\text{neg}} \\ 0, & i \in \mathcal{I}^{\text{sep}} \end{cases}$$

$$D_{e,i\pm0.5}^{\text{eff}} = (\Delta\delta_i + \Delta\delta_{i+1})/\left(\frac{\Delta\delta_i}{D_{e,i}^{\text{eff}}} + \frac{\Delta\delta_{i\pm1}}{D_{e,i\pm1}^{\text{eff}}} \right),$$

where $D_{e,i}^{\text{eff}}$ is the effective electrolyte diffusion coefficient, t_a^0 is the transference number, and $\varepsilon_{e,i}$ is the porosity.

4) Update of Temperature State: In addition, battery temperature T is described by a lumped heat transfer model, i.e.,

$$\dot{T} = \frac{T_{\text{amb}} - T}{R_T C_T} + \frac{Q_T}{C_T} = \frac{T_{\text{amb}} - T}{R_T C_T} + \frac{Q_{\text{rxn}} + Q_{\text{rev}} + Q_{\text{ohm}}}{C_T}, \quad (14)$$

where C_T is the thermal capacitance, R_T is the thermal resistance, and T_{amb} is the ambient temperature. The heat generation Q_T consists of the reaction heat Q_{rxn}, reversible heat Q_{rev}, and ohmic heat Q_{ohm}, and it can be calculated as the total power losses (including reversible heat generation) of the equivalent circuit network in Fig. 1, given by [23]

$$Q_{\text{rxn}} = \sum_{i \in \mathcal{I}^{\text{pos}} \cup \mathcal{I}^{\text{neg}}} R_{\Sigma,i} I_{n,i}^2, \quad (15)$$

$$Q_{\text{rev}} = \sum_{i \in \mathcal{I}^{\text{pos}} \cup \mathcal{I}^{\text{neg}}} I_{n,i} T \left(\frac{\partial U}{\partial T} \right)_i, \quad (16)$$

$$Q_{\text{ohm}} = \sum_{i \in \mathcal{I}'} \left(R_{e,i+0.5} I_{e,i+0.5}^2 + R_{s,i+0.5} I_{s,i+0.5}^2 \right)$$
$$+ (R_e^{\text{sep}} + R_{\text{col}}) I_{\text{app}}^2 + \sum_{i \in \mathcal{I}^{\text{pos}} \cup \mathcal{I}^{\text{neg}}} I_{n,i} U_{e,i}. \quad (17)$$

Plugging (1)–(3), (8), and (15)–(17) into (4)–(7) and (9)–(14), we obtain a system of ordinary differential equations in the form

$$\dot{x} = f(x, u) \quad (18a)$$
$$y = g(x, u) \quad (18b)$$

where $x \in \mathbb{R}^{n_x}$ is the state vector containing all $\tilde{c}_{s,i,m}$, $c_{e,i}$, and T, $u = I_{\text{app}} \in \mathbb{R}$ is the input, and $y \in \mathbb{R}^{n_y}$ is the output vector. $f : \mathbb{R}^{n_x} \times \mathbb{R} \to \mathbb{R}^{n_x}$ and $g : \mathbb{R}^{n_x} \times \mathbb{R} \to \mathbb{R}^{n_y}$ are two nonlinear operators on x and u. The output vector is defined based on the selection of constraints on battery charging, which will be discussed next.

B. Typical Constraints for Battery Fast Charging

The charging current rate of a Li-ion battery can be limited by several factors. First, the terminal power, voltage, and current of the battery are usually limited by the power rating, the

maximum voltage, and current rating of the power electronic devices, i.e.,

$$I_{\text{app}} \le \overline{I}_{\text{app}} \quad (19a)$$
$$V_{\text{bat}} \le \overline{V}_{\text{bat}} \quad (19b)$$
$$P_{\text{bat}} \le \overline{P}_{\text{bat}}, \quad (19c)$$

where the overbar represents the upper limit.

Second, a large amount of heat generated during the fast charging can cause high temperature rise and safety issues such as thermal runaway can be triggered. Hence, it is necessary to place an upper limit on temperature,

$$T \le \overline{T}. \quad (19d)$$

Third, during charging, the side reactions of LiP in the negative electrode tend to accelerate the aging of the battery under high current rates. To restrain the battery aging due to LiP on the whole negative electrode, it is sufficient to impose a constraint only to the negative electrode/separator interface as follows [27]

$$-\eta_{\text{LiP}}^{\text{sep/neg}} \le -\underline{\eta}_{\text{LiP}} < 0, \quad (19e)$$

where $\eta_{\text{LiP}}^{\text{sep/neg}}$ is the lithium plating potential at the separator/negative electrode interface and the underline represents the lower limit.

In some cases, we also hope to avoid rapid growth of the SEI resistance by limiting its side-reaction molar flux:

$$0 < -j_{\text{SEI}}^{\text{sep/neg}} \le -\underline{j}_{\text{SEI}}. \quad (19f)$$

Next, we may hope to limit the solid-phase concentrations in the negative electrode to avoid local overcharging. This can be ensured by

$$c_{\text{ss}}^{\text{sep/neg}} \le \overline{c}_{\text{ss}}^{\text{neg}} < c_{s,\text{max}}^{\text{neg}}, \quad (19g)$$

where $c_{\text{ss}}^{\text{sep/neg}}$ is the solid-phase surface concentration at the separator/negative electrode interface.

Also, to avoid the depletion of lithium ions in the electrolyte, we would apply

$$-c_e^{\text{neg/col}} \le -\underline{c}_e < 0 \quad \forall i \in \mathcal{I}^{\text{pos}} \cup \mathcal{I}^{\text{sep}} \cup \mathcal{I}^{\text{neg}}, \quad (19h)$$

where $c_e^{\text{neg/col}}$ is the electrolyte concentration at the negative electrode/current collector interface.

Last but not least, to avoid the overcharging in a bulk manner,

$$\text{SOC} \le \text{SOC}_f \quad (19i)$$

must hold, where SOC_f is the targeted final SOC.

We denote the above-mentioned constraint-related variables by an output vector

$$y = [I_{\text{app}}, V_{\text{bat}}, P_{\text{bat}}, T, -\eta_{\text{LiP}}^{\text{sep/neg}}, -j_{\text{SEI}}^{\text{sep/neg}}, c_{\text{ss}}^{\text{sep/neg}},$$
$$- c_e^{\text{neg/col}}, \text{SOC}]^\top, \quad (20a)$$

and the corresponding upper bounds are defined as

$$y^* = [\overline{I}_{\text{app}}, \overline{V}_{\text{bat}}, \overline{P}_{\text{bat}}, \overline{T}, -\underline{\eta}_{\text{LiP}}, -\underline{j}_{\text{SEI}}, \overline{c}_{\text{ss}}^{\text{neg}} - \underline{c}_e, \text{SOC}_f,]^\top \quad (20b)$$

Note that the bounds y^* can be time-varying, depending on the operating conditions and battery aging conditions. For

example, the power rating $\overline{P}_{\text{bat}}$ can be specified according to vehicle-to-grid or smart charging requirements. For aged batteries, we might impose a reduced temperature limit $\overline{T}$ to reduce the increased risk of thermal runaway. Nevertheless, the determination and discussion of y^* is not the focus of the present investigation and we assume they are constant in this work.

It should also be noted that in the FVM, the boundary values, including $\eta_{\text{LiP}}^{\text{sep/neg}}$, $j_{\text{SEI}}^{\text{sep/neg}}$, $c_{\text{ss}}^{\text{sep/neg}}$, and $c_e^{\text{neg/col}}$, are usually interpolated as a linear combination of the calculated local values near the boundary. For simplicity, we use the two-point interpolation as follows

$$\eta_{\text{LiP}}^{\text{sep/neg}} = \frac{3}{2}\eta_{\text{LiP},i}|_{i=N^{\text{sep/neg}}} - \frac{1}{2}\eta_{\text{LiP},i}|_{i=N^{\text{sep/neg}}+1} \quad (21a)$$

$$j_{\text{SEI}}^{\text{sep/neg}} = \frac{3}{2}j_{\text{SEI},i}|_{i=N^{\text{sep/neg}}} - \frac{1}{2}j_{\text{SEI},i}|_{i=N^{\text{sep/neg}}+1} \quad (21b)$$

$$c_{\text{ss}}^{\text{sep/neg}} = \frac{3}{2}c_{\text{ss},i}|_{i=N^{\text{sep/neg}}} - \frac{1}{2}c_{\text{ss},i}|_{i=N^{\text{sep/neg}}+1} \quad (21c)$$

$$c_e^{\text{neg/col}} = \frac{3}{2}c_{e,i}|_{i=N^{\text{tot}}} - \frac{1}{2}c_{e,i}|_{i=N^{\text{tot}}-1}. \quad (21d)$$

III. GENERAL OPTIMAL CONTROL PROBLEM FOR BATTERY FAST CHARGING

The problem of optimally fast charging a battery has been well-discussed in [14]. A general time-optimal control problem can be formulated as follows. Suppose the battery is charging from a given initial state x_0 at time t_0. The charging process will end at time t_f when the charge level has reached the target final state of charge SOC_f. The optimal fast charging profile is obtained by solving

Problem 1 (General Fast Charging Problem):

$$\min_{u(t), t \in [t_0, t_f]} \int_{t_0}^{t_f} 1\, dt \quad (22a)$$

$$\text{s.t.} \quad \text{state equation} \quad \dot{x}(t) = f(x(t), u(t)), \quad (22b)$$

$$\text{output equation} \quad y(t) = g(x(t), u(t)), \quad (22c)$$

$$\text{initial state} \quad x(t_0) = x_0, \quad (22d)$$

$$\text{final SOC} \quad \text{SOC}(t_f) = \text{SOC}_f, \quad (22e)$$

$$\text{inequality constraints} \quad y(t) \leq y^*, \quad (22f)$$

where x, u, y, f, g, and t are system state, input, output, state function, output function, and continuous time instant, respectively. We use y_j, y_j^*, and g_j to denote the jth element of y, y^*, and g, respectively, where $j \in \{1, 2, \cdots, n_y\}$. Note that in contrast to the common formulation in the literature, we also treat the input u as an output and it is defined as the first element in y. This gives $y_1 = u$ and $y_1^* = \overline{u}$, where $\overline{u}$ is the upper limit of the input (i.e., $\overline{I}_{\text{app}}$).

Unfortunately, as discussed in [14], this general fast charging problem is difficult to solve analytically as a battery model is usually highly nonlinear and subject to many state/output constraints. However, based on a numerically obtained approximate global solution, it is shown in [14] that Problem 1 can be well addressed via NMPC, i.e., at each control instance $t \in [0, \Delta t, 2\Delta t, \cdots, t_f - \Delta t]$ the following nonlinear optimization problem with a reduced optimization horizon $[t, t+H]$ is solved:

Problem 2 (NMPC-Based Fast Charging):

$$u^\star(t) = \operatorname*{arg\,min}_{u(t), t \in [t_k, t_k+H]} - \int_{t_k}^{t_k+H} u(t)dt \quad (23)$$

$$\text{s.t.} \quad \text{the same constraints as (22b)–(22f)},$$

and only a part of the solution $u^\star(t), t \in [t_k, t_k + \Delta t]$ is applied.

For the fast charging problem under the conditions of extremely high current and wide temperature ranges, considerable nonuniform battery dynamics can be excited so that a high-dimensional nonlinear model is essential to guarantee the prediction accuracy [30]. For short prediction horizons, the fast charging problem (23) can also be solved via the LTV-MPC. However, in the presence of hundreds of battery cells in a battery pack, the cell inconsistency problem needs also to be properly addressed when designing the control algorithm. In this condition, the complexity and computational burden of an MPC solver for battery systems may increase dramatically.

IV. NONLINEAR INVERSION-BASED OUTPUT TRACKING CONTROL FOR BATTERY FAST CHARGING

A. Output Tracking with Multiple References

To cope with the challenge of high computation of MPC-based solution, we first consider a relaxed problem similar to Problem 2, but with only the first (regarding the input) and the jth inequality constraints imposed. We denote this problem as Problem 3.j. For Problem 3.1 where only the input constraint is imposed, we have

Problem 3.1 (Input-Bounded Fast Charging):

$$u^\star(t) = \operatorname*{arg\,min}_{u(t), t \in [t_k, t_k+H]} - \int_{t_k}^{t_k+H} u(t)dt \quad (24a)$$

$$\text{s.t.} \quad \text{the same constraints as (22b)–(22e)},$$

$$u(t) \leq \overline{u} \quad (24b)$$

We can immediately obtain the solution as $u(t) \equiv \overline{u}$. The corresponding charging time can be approximated as $3600\mathcal{Q}_{\text{max}}(\text{SOC}_f - \text{SOC}_0)/(\eta\overline{u})$ given by coulomb counting

$$\dot{\text{SOC}} = \eta I_{\text{app}}/(3600\mathcal{Q}_{\text{max}}), \quad (25)$$

where η is the coulombic efficiency and $\mathcal{Q}_{\text{max}}$ is the battery capacity in ampere-hour (Ah).

Next, consider Problem j where $j \in \{2, 3, \cdots, n_y\}$, i.e., *Problem 3.j (Input-Output-Bounded Fast Charging)*:

$$u^\star(t) = \operatorname*{arg\,min}_{u(t), t \in [t_k, t_k+H]} - \int_{t_k}^{t_k+H} u(t)dt \quad (26a)$$

$$\text{s.t.} \quad \text{the same constraints as (22b)–(22e)},$$

$$u(t) \leq \overline{u} \quad (26b)$$

$$y_j(t) \leq y_j^* \quad (26c)$$

In this case, one more constraint is imposed along with the input constraint and thus the corresponding optimal current is always less or equal to that of Problem 3.1. In other words, the optimal solution to Problem 3.j should always be in the feasible domain of Problem 3.1. In this condition, to guarantee the compliance with the inequality constraints, the optimal

output should always track one of the upper bounds y_j^*. We thus propose to design a simple control strategy as

$$I_{\text{app}}^*(t) = u^*(x(t), y^*)$$
$$\equiv \min\{u_j^*(x(t), y_j^*) : j = 1, 2, \cdots, n_y\}, \quad (27)$$

where u_j^* is the solution for the output y_j to track its reference (constraint) y_j^*. This general control strategy converts an optimal control problem to an output tracking problem with multiple tracking objectives y_j^*, where we should apply the lowest current to charge the battery. We notice that this result is in agreement with that in [34], where the authors proved that based on an SPM, the optimal fast charging protocol follows a "bang-ride" control law where the control trajectory always sits on a constraint.

Inversion-based techniques [35] will next be used to solve the output tracking problem. We notice that for the battery model under investigation, all the output variables y_j, or their first time-derivatives $\dot{y}_j$, can be expressed in a low-degree input-polynomial form, as will be shown in Section V. Based on this fact, we will first analyze and derive a control strategy based on whether or not the input u has direct feedthrough to the output y_j or not. For brevity, the time argument t will be dropped henceforth.

B. Inversion Law: Input With Direct Feedthrough to the Output

When the input u has a direct feedthrough to an output y_j, we express y_j in the following input-polynomial form (either through analytical derivation or through approximation):

$$y_j = g_j(x, u) = \sum_{l=0}^{L_j} h_j^{[l]}(x)u^l$$
$$= h_j^{[0]}(x) + h_j^{[1]}(x)u + \cdots + h_j^{[L_j]}(x)u^{L_j}, \quad (28)$$

where $h_j^{[l]} : \mathbb{R}^{n_x} \to \mathbb{R}$ represents the lth polynomial coefficient (function) for the jth output variable and $L_j \in \{1, 2, 3, \cdots\}$ represents the degree of the polynomial. We note that $h_j^{[l]}$ is a state-dependent coefficient (SDC).

Given the reference output $y_j = y_j^*$, we seek the solution $u = u_j^* = g_j^{-1}(x, y_j^*)$, based on (28), by inversion. Analytical solutions exist and are easy to obtain for a low-degree polynomial. For example, when $L_j = 1$, (28) becomes input-affine, and the required control input u_j^* is

$$u_j^* = \frac{y_j^* - h_j^{[0]}(x)}{h_j^{[1]}(x)}. \quad (29)$$

where $h_j^{[1]}(x) \neq 0$.

If $L_j = 2$, (28) becomes an input-quadratic form. For the charging process, given $y_j = y_j^*$, the required input is the nonnegative solution to a quadratic equation, i.e.,

$$u_j^* = \frac{-h_j^{[1]}(x) + \sqrt{(h_j^{[1]}(x))^2 - 4h_j^{[2]}(x)(h_j^{[0]}(x) - y_j^*)}}{2h_j^{[2]}(x)}. \quad (30)$$

where $h_j^{[2]}(x) \neq 0$.

For $L_j = 3$, the analytical solution exists, although the expression is rather complex. When $L_j > 3$, there is no general analytical solutions [36]. Fortunately, we will show that input-polynomial forms with $L_j \geq 3$ are not needed in the present study on battery charging control.

C. Inversion Law: Input Without Direct Feedthrough to the Output

Note that if $L_j = 0$ in (28) for an output, the input has no direct feedthrough to it, and the output will be a function of the states x only. In this condition, instead of investigating (28), we consider the first time-derivative of y_j. Similarly to (28), we assume $\dot{y}_j$ can be expressed in an input-polynomial form:

$$\dot{y}_j = \dot{g}_j(x, u) = \sum_{l=0}^{L_j'} h_j^{[l]}(x)u^l, \quad (31)$$

where $L_j' \in \{1, 2, 3, \cdots\}$ is the degree of the polynomial function.

Clearly, to achieve $y_j = y_j^*$ at all times, a direct inversion of the input-output relationship (31) requires unfavorable differential operation for practical implementation. To avoid the differential operation and achieve zero-offset control, we propose to shape the relationship between y_j^* and y_j as a first-order system with a unit gain, i.e.,

$$\tau_j \dot{y}_j = -y_j + y_j^* \quad (32)$$

where the time constant τ_j is a tuning parameter. In this way, the output variable can exponentially approach its upper bound in a monotonic manner without generating an overshoot. Substituting (31) into (32) yields

$$\frac{y_j^* - y_j(x)}{\tau_j} = \sum_{l=0}^{L_j'} h_j^{[l]}(x)u^l. \quad (33)$$

We can then solve (33) for u based on the polynomial degree L_j', and similar results to (29) and (30) can be obtained. Specifically, if $L_j' = 1$, (31) possesses an input-affine form, and the required control input is

$$u_j^* = \frac{\frac{y_j^* - y_j(x)}{\tau_j} - h_j^{[0]}(x)}{h_j^{[1]}(x)}. \quad (34)$$

If $L_j' = 2$, (31) has an input-quadratic form, and the required nonnegative control input for battery charging is

$$u_j^* = \frac{-h_j^{[1]}(x) + \sqrt{(h_j^{[1]}(x))^2 - 4h_j^{[2]}(x)(h_j^{[0]}(x) - \frac{y_j^* - y_j(x)}{\tau_j})}}{2h_j^{[2]}(x)}. \quad (35)$$

D. Overall Control Framework and Some Remarks

The proposed charging control algorithm based on nonlinear model inversion is summarized as Alg. 1. Note that the inversion-based control generally assumes that exact model parameters are known [37], which can be identified using online or offline methods. In order to improve the robustness of the algorithm to model errors, as shown in Fig. 2, a PI

Algorithm 1 Nonlinear Inversion-Based Output Tracking Control for Battery Fast Charging

1: At $t = t_0$, initialize the ensemble-based state estimator.
2: **while** $t > t_0$ and SOC $<$ SOC$_f$ **do**
3:    Obtain measurements.
4:    Estimate the state x using a state estimator.
5:    Set $j = 1$.
6:    **while** $j \leq n_y$ **do**
7:       Specify y_j^*.
8:       Calculate the SDCs $h_j^{[0]}(x)$, $h_j^{[1]}(x)$, and $h_j^{[2]}(x)$.
9:       Calculate u_j^* using (29), (30), (34), or (35).
10:       Set $j = j + 1$.
11:    **end while**
12:    Calculate the charging current I_{app}^* with (27).
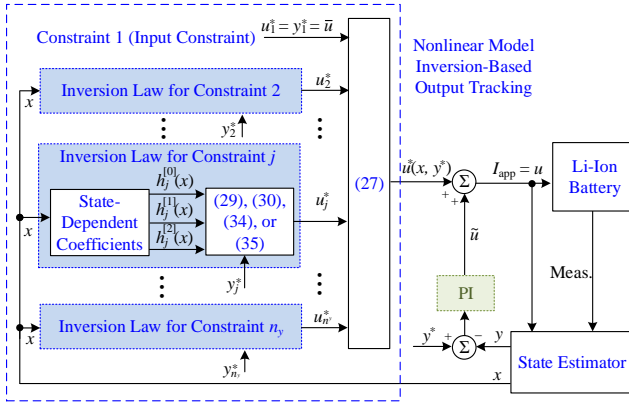13:   Forward t.
14: **end while**

Fig. 2. Block diagram of the proposed nonlinear inversion-based output tracking (Algorithm 1) with a PI-based feedback control for fast charging of Li-ion batteries.

controller (such as PCT-PI [27]) can be integrated. As shown in Fig. 2, the inversion-based control essentially computes the nominal tracking control command u^*, which can be viewed as a feedforward (FF) component. On the other hand, the PI controller generates a fraction $\tilde{u}$. Compared to the scheme with PI control only, the tuning of PI parameters with FF is less performance-wise, as the PI control only needs to address the perturbation due to model mismatch (i.e., the PI output $\tilde{u} = 0$ if the model is perfect). For single-input and single-output cases, such a combination of PI and FF controls is generally superior to either the pure FF or pure PI control [37].

Note that since the nominal input u^* is a nonlinear function of state x, parameterized by the reference y^*, the proposed inversion-based control can also be viewed as nonlinear state feedback control. Hence, the state x must be fully observable and a state observer/estimator is needed. However, for the sake of brevity, state estimation is not further elaborated in the present work, and we assume direct access to x during the analysis. The effect of state estimation on control performance will be examined in Section VI-E.

Next, we will show that all the output variables in (20a) can

be tracked using the proposed inversion method.

V. STATE-DEPENDENT COEFFICIENTS FOR INVERSION-BASED OUTPUT TRACKING

In Section II-A and Appendix A, we show that the following quantities are state-dependent variables: Resistances ($R_{e,i+0.5}$, $R_{s,i+0.5}$, R_e^{sep}), voltage sources ($U_{ss,i}$ and $U_{e,i}$), the ZIR components in branch currents ($I_{n,i}^{ZIR}$, $I_{e,i+0.5}^{ZIR}$, $I_{s,i+0.5}^{ZIR}$), the gain of the ZSR components in the branch currents ($K_{n,i}^{ZSR}$, $K_{e,i+0.5}^{ZSR}$, $K_{s,i+0.5}^{ZSR}$), concentrations ($c_{ss,i}$, $c_{s,avg,i}$, $c_{e,i}$, $c_{ss}^{sep/neg}$, $c_e^{neg/col}$), temperature T, and SOC. Parameters such as $D_{s,i}^{eff}$ and/or $D_{e,i}^{eff}$ are also functions of concentrations and temperature (see Table A1 in Appendix. To this end, our task is to derive the SDC expressions $h_j^{[l]}(x)$ for each output y_j in (20a).

A. Constant Current Control ($j = 1$)

Since the current is the model input, it is a special case for (28), with $L_1 = 1$, $h_1^{[0]}(x) \equiv 0$ and $h_1^{[1]}(x) \equiv 1$. The control signal is simply the maximum current, i.e., $u_1^* = y_1^* = \bar{I}_{app}$. This is thus an open-loop control.

B. Constant Voltage Control ($j = 2$)

Substituting (1) and (2) into (4), the battery voltage can be expressed in the form of (28) with $L_2 = 1$. Considering $y_2^* = \overline{V}_{bat}$ in (29), we obtain the control signal to achieve CV tracking:

$$u_2^* = \frac{\overline{V}_{bat} - h_2^{[0]}(x)}{h_2^{[1]}(x)} \tag{36}$$

where

$$
\begin{aligned}
h_2^{[0]}(x) &= (U_{ss,1} + U_{e,1} + R_{\Sigma,1} I_{n,1}^{ZIR}) - \\
&\quad (U_{ss,N^{tot}} + U_{e,N^{tot}} + R_{\Sigma,N^{tot}} I_{n,N^{tot}}^{ZIR}) + \\
&\quad + \sum_{i \in \mathcal{I}'} R_{e,i+0.5} I_{e,i+0.5}^{ZIR} \\
h_2^{[1]}(x) &= K_{n,1}^{ZSR} R_{\Sigma,1} - K_{n,N^{tot}}^{ZSR} R_{\Sigma,N^{tot}} \\
&\quad + \sum_{i \in \mathcal{I}'} K_{e,i+0.5}^{ZSR} R_{e,i+0.5} + R_e^{sep}.
\end{aligned}
$$

C. Constant Power Control ($j = 3$)

Since the battery power is the product of the terminal voltage and the applied current, it can be derived that

$$
\begin{aligned}
P_{bat} \equiv y_3 &= [h_2^{[0]}(x) + h_2^{[1]}(x)u]u \\
&= h_3^{[0]}(x) + h_3^{[1]}(x)u + h_3^{[2]}(x)u^2. \tag{37}
\end{aligned}
$$

Hence, considering $y_3^* = \overline{P}_{bat}$ in (30), we can obtain the CP control law

$$u_3^* = \frac{-h_4^{[1]}(x) + \sqrt{[h_3^{[1]}(x)]^2 - 4h_3^{[2]}(x)[h_3^{[0]}(x) - \overline{P}_{bat}]}}{2h_3^{[2]}(x)} \tag{38}$$

where

$$
\begin{aligned}
h_3^{[0]}(x) &= 0 \\
h_3^{[1]}(x) &= h_2^{[0]}(x) \\
h_3^{[2]}(x) &= h_2^{[1]}(x).
\end{aligned}
$$

D. Constant Temperature Control ($j = 4$)

In contrast to the output variables described in Section V-A to Section V-C, the battery temperature T is a state variable. First, by substituting the expressions of the branch currents (1)–(3) into (15)–(17), the heat generation Q_T can be expressed in a quadratic form w.r.t. the input $u = I_{\text{app}}$:

$$Q_T = Q_Q(x) + V_Q(x)I_{\text{app}} + R_Q(x)I_{\text{app}}^2 \qquad (39)$$

where the coefficients $Q_Q(x)$, $V_Q(x)$, and $R_Q(x)$ are state-dependent functions in the units of power, voltage, and resistance, respectively, and their expressions are provided in Appendix B. Substituting (39) into (14), letting $y_4 = T$ and $y_4^* = \overline{T}$, and considering (35), the constant temperature (CT) control is achieved by

$$u_4^* = \frac{-h_4^{[1]}(x) + \sqrt{[h_4^{[1]}(x)]^2 - 4h_4^{[2]}(x)[h_4^{[0]}(x) - \frac{\overline{T} - T}{\tau_4}]}}{2h_4^{[2]}(x)}$$
$$(40)$$

where the time constant τ_4 is control parameter and

$$h_4^{[0]}(x) = \frac{T_{\text{amb}} - T}{R_T C_T} + \frac{Q_Q(x)}{C_T},$$
$$h_4^{[1]}(x) = \frac{V_Q(x)}{C_T}, \quad h_4^{[2]}(x) = \frac{R_Q(x)}{C_T}.$$

E. Constant Lithium-Plating Potential Control ($j = 5$)

As mentioned in Section II-B, it is sufficient to limit the LiP at the separator/negative electrode interface. By substituting (1) into (6) and considering $y_5^* = -\underline{\eta}_{\text{LiP}}$ in (29), we can obtain the control signal to achieve constant LiP ($C\eta_{LiP}$) control:

$$u_5^* = \frac{-\underline{\eta}_{\text{LiP}} - h_5^{[0]}(x)}{h_5^{[1]}(x)}, \qquad (41)$$

where

$$h_{5,i}^{[0]}(x) = -U_{\text{ss},i} - I_{n,i}^{\text{ZIR}} R_{\Sigma,i}$$
$$h_{5,i}^{[1]}(x) = -K_{n,i}^{\text{ZSR}} R_{\Sigma,i}$$
$$h_5^{[0]}(x) = \frac{3}{2}h_{5,i}^{[0]}|_{i=N^{\text{sep/neg}}} - \frac{1}{2}h_{5,i}^{[0]}|_{i=N^{\text{sep/neg}}+1}$$
$$h_5^{[1]}(x) = \frac{3}{2}h_{5,i}^{[1]}|_{i=N^{\text{sep/neg}}} - \frac{1}{2}h_{5,i}^{[1]}|_{i=N^{\text{sep/neg}}+1}.$$

F. Constant SEI Reaction Rate Control ($j = 6$)

Recall that the SEI side reactions are described by (7) and (8). To limit the SEI film growth, an additional step is needed for deriving the inversion law. According to (8), instead of treating $j_{\text{SEI},i}$ as the output y_6 as in Section II-B, we define y_6 as follows:

$$y_6 := \ln\left(\frac{-j_{\text{SEI},i}}{\mathcal{F}i_{0,\text{SEI}}}\right) = -\frac{\mathcal{F}}{2\mathcal{R}T}\eta_{\text{SEI},i}. \qquad (42)$$

Substituting (7) and (1) into the above equation yields

$$y_6 = -\frac{\mathcal{F}}{2\mathcal{R}T}[U_{\text{ss},i} + R_{\text{ct},i}(I_{n,i}^{\text{ZIR}} + K_{n,i}^{\text{ZSR}}I_{\text{app}}) - U_{\text{SEI}}]. \qquad (43)$$

Thus, the input has direct feedthrough to y_6. According to (29), we have the following constant SEI reaction rate (Cj_{SEI}) control:

$$u_6^* = \frac{\overline{y}_6 - h_6^{[0]}(x)}{h_6^{[1]}(x)}, \qquad (44)$$

where the coefficients are

$$h_6^{[0]}(x) = -\frac{\mathcal{F}}{2\mathcal{R}T}(U_{\text{ss},i} + R_{\text{ct},i}I_{n,i}^{\text{ZIR}} - U_{\text{SEI}}),$$
$$h_6^{[1]}(x) = -\frac{\mathcal{F}}{2\mathcal{R}T}(R_{\text{ct},i}K_{n,i}^{\text{ZSR}}),$$

and the reference $\overline{y}_9 = \ln\left(\frac{-\underline{j}_{\text{SEI}}}{\mathcal{F}i_{0,\text{SEI}}}\right)$ is related to the allowable maximum SEI side reaction rates $-\underline{j}_{\text{SEI}}$.

G. Constant Solid-Phase Surface Concentration Control ($j = 7$)

The solid-phase concentration $c_{\text{ss},i}$ is a state-dependent variable. The time derivatives of $c_{\text{ss},i}$ and $c_{\text{ss}}^{\text{sep/neg}}$ can be derived using (1), (9), and (10), i.e.,

$$\dot{c}_{\text{ss},i} = \sum_{m=1}^{M} \dot{\tilde{c}}_{s,i,m} = -\frac{D_{s,i}^{\text{eff}}}{R_{p,i}^2}\sum_{m=1}^{M}(\alpha_m \tilde{c}_{s,i,m})$$

Considering $y_7^* = \overline{c}_{\text{ss}}^{\text{neg}}$, $y_7 = c_{\text{ss}}^{\text{sep/neg}}$, and using (34) and (21c), we have constant solid-phase surface concentration (Cc_{ss}) control

$$u_7^* = \frac{\frac{\overline{c}_{\text{ss}}^{\text{neg}} - c_{\text{ss}}^{\text{sep/neg}}(x)}{\tau_7} - h_7^{[0]}(x)}{h_7^{[1]}(x)}, \qquad (45)$$

where the time constant τ_7 is a control parameter and

$$h_{7,i}^{[0]}(x) = -\frac{D_{s,i}^{\text{eff}}}{R_{p,i}^2}\sum_{m=1}^{M}(\alpha_m \tilde{c}_{s,i,m}) - \frac{1}{R_{p,i}}\frac{I_{n,i}^{\text{ZIR}}}{\mathcal{F}A\Delta\delta_i a_{s,i}}\sum_{m=1}^{M}\beta_m$$
$$h_{7,i}^{[1]}(x) = -\frac{1}{R_{p,i}}\frac{K_{n,i}^{\text{ZSR}}}{\mathcal{F}A\Delta\delta_i a_{s,i}}\sum_{m=1}^{M}\beta_m$$
$$h_7^{[0]}(x) = \frac{3}{2}h_{7,i}^{[0]}|_{i=N^{\text{sep/neg}}} - \frac{1}{2}h_{7,i}^{[0]}|_{i=N^{\text{sep/neg}}+1}$$
$$h_7^{[1]}(x) = \frac{3}{2}h_{7,i}^{[1]}|_{i=N^{\text{sep/neg}}} - \frac{1}{2}h_{7,i}^{[1]}|_{i=N^{\text{sep/neg}}+1}.$$

H. Constant Electrolyte Concentration Control ($j = 8$)

The electrolyte concentration $c_e^{\text{neg/col}}$ is state-dependent. We can therefore use (34), (1), (10), (13), and (21d) to obtain its inversion law for constant electrolyte concentration (Cc_e) control:

$$u_8^* = \frac{\frac{-\underline{c}_e + c_e^{\text{neg/col}}(x)}{\tau_8} - h_8^{[0]}(x)}{h_8^{[1]}(x)} \qquad (46)$$

where τ_8 is a control parameter and

$$h_{8,i}^{[0]} = -\frac{1}{\Delta\delta_i \varepsilon_{e,i}} \left(\frac{D_{e,i+0.5}^{\text{eff}}}{0.5} \frac{c_{e,i+1} - c_{e,i}}{\Delta\delta_{i+1} + \Delta\delta_i} - \right.$$

$$\left. \frac{D_{e,i-0.5}^{\text{eff}}}{0.5} \frac{c_{e,i} - c_{e,i-1}}{\Delta\delta_{i-1} + \Delta\delta_i} \right) - \frac{t_a^0}{\varepsilon_{e,i}} \frac{I_{n,i}^{\text{ZIR}}}{\mathcal{F}A\Delta\delta_i}$$

$$h_{8,i}^{[1]} = -\frac{t_a^0}{\varepsilon_{e,i}} \frac{K_{n,i}^{\text{ZSR}}}{\mathcal{F}A\Delta\delta_i},$$

$$h_8^{[0]}(x) = \frac{3}{2} h_{8,i}^{[0]}|_{i=N^{\text{tot}}} - \frac{1}{2} h_{8,i}^{[0]}|_{i=N^{\text{tot}}-1}$$

$$h_8^{[1]}(x) = \frac{3}{2} h_{8,i}^{[1]}|_{i=N^{\text{tot}}} - \frac{1}{2} h_{8,i}^{[1]}|_{i=N^{\text{tot}}-1}.$$

I. Constant SOC Control ($j = 9$)

According to (11) and (12), the battery SOC is a state-dependent variable. By defining the capacity $\mathcal{Q}_{\max} = \sum_{i\in\mathcal{I}^{\text{neg}}}[(c_{s,100\%}^{\text{neg}} - c_{s,0\%}^{\text{neg}})\mathcal{F}A\Delta\delta_i\varepsilon_{s,i}]/(3600\eta)$ where $\varepsilon_{s,i} = a_{s,i}R_{p,i}/3$, one can use (9), (12), and the fact $\sum_{i\in\mathcal{I}^{\text{neg}}} I_{n,i} = -I_{\text{app}}$, to derive (25).

From (25) and (34) and considering $y_9^* = \text{SOC}_f$ and $y_9 = \text{SOC}$, we then have constant SOC (CSOC) control

$$u_9^* = \frac{\frac{\text{SOC}_f - \text{SOC}(x)}{\tau_9} - h_9^{[0]}(x)}{h_9^{[1]}(x)} \qquad (47)$$

where the time constant τ_9 is a control parameter and

$$h_9^{[0]}(x) = 0$$
$$h_9^{[1]}(x) = 1/(3600\mathcal{Q}_{\max}).$$

VI. ILLUSTRATIVE EXAMPLES

A. System Configuration

In this section, results from simulation studies will be presented to verify the efficacy of the proposed control strategy. The battery model and controller are both implemented in MATLAB R2016a, and the simulated results were obtained on a 64-bit Windows 10 on a PC with Intel Core 2 Q9400 @ 2.67GHz processor and 8GB RAM. We consider evenly divided control volumes in each domain, and the numbers of control volumes of the battery model are selected to be high to guarantee the model fidelity under high-current and high-temperature conditions, i.e., $N^{\text{pos}} = N^{\text{neg}} = 10$ and $N^{\text{sep}} = 3$. For the solid-phase diffusion equations (9)–(11), a 2nd-order model ($M = 2$) is adopted, which gives $\alpha_1 = 0, \beta_1 = 3, \alpha_2 = 35$, and $\beta_2 = 7$. The parameters of the battery model are described in Appendix C. To simulate the battery process, the battery model is solved using the continuous-time solver ode23ts with guaranteed numerical stability for such a stiff system. For the controller, under the assumption of perfect state estimation, the plant state x is sampled at $\Delta t = 1$ s.

B. Performance of the Inversion-Based Output Tracking for Battery Charging

Three examples of the simulated current profile based on the proposed inversion-based fast charging strategy are shown in
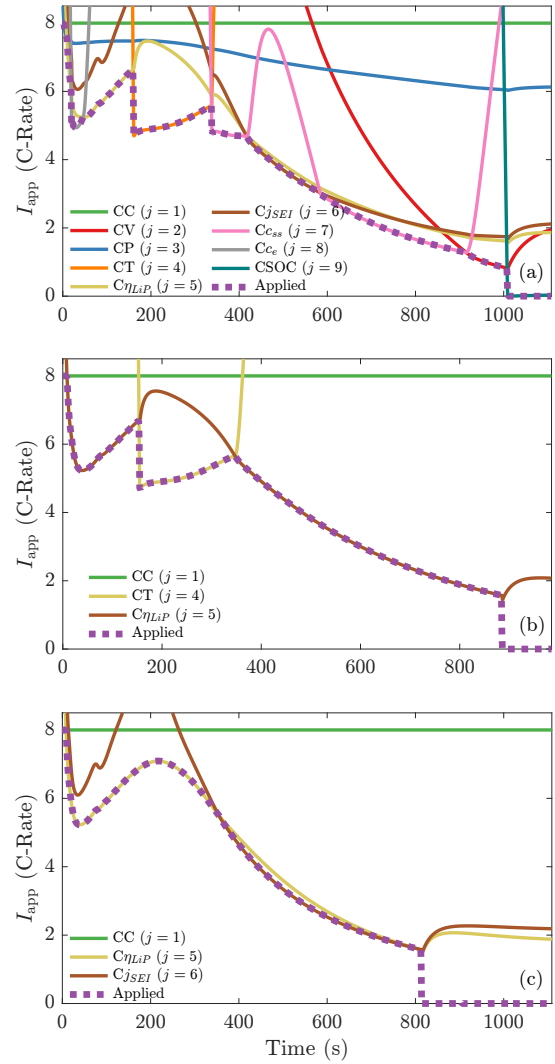

Fig. 3. Examples of candidate and applied charging current profiles. (a) All nine physical constraints are imposed. (b) CC-CT-Cη_{LiP} control. (c) CC-Cη_{LiP}-Cj_{SEI} control.

Fig. 3, where the calculated input u_j^* for each constraint is also plotted and indicated by the output index j. In the first example as shown in Fig. 3(a), all nine inequality constraints described in Section V are imposed for demonstration purposes. The constraints for the control are: $\overline{I}_{\text{app}}/\mathcal{Q}_{\max} = 8\text{C}$, $\overline{V}_{\text{bat}} = 4.4$ V, $\overline{P}_{\text{bat}} = 70$ W, $\overline{T} = 323.15$ K (50 °C), $\eta_{\text{LiP}} = 0$ V, and $\underline{j}_{\text{SEI}} = -4.6 \times 10^{-8}$ mol/(m^2 · s), $\overline{c}_{ss}^{\text{neg}} = 0.98c_{s,\max}^{\text{neg}}$, and $\underline{c}_e = 0.25c_e^0$. The battery is charged from the fully empty state to the fully charged state, i.e., $\text{SOC}_0 = 0$, $\text{SOC}_f = 1$. Furthermore, we select the time constants as $\tau_4 = \tau_7 = \tau_8 = \tau_9 = 1$ s. In practice, only a subset of the constraints may be needed. For example, in the second and third cases as shown in Figs. 3(b) and (c), only part of the constraints are imposed, leading to the CC-CT-Cη_{LiP} control and CC-Cη_{LiP}-Cj_{SEI} control, respectively. It can be observed from Fig. 3 that all the candidate currents and the final applied current profile are affected by how the constraints are selected.

Fig. 4 shows the LiP potentials, solid-phase concentrations at particle surfaces, electrolyte concentrations, temperature,
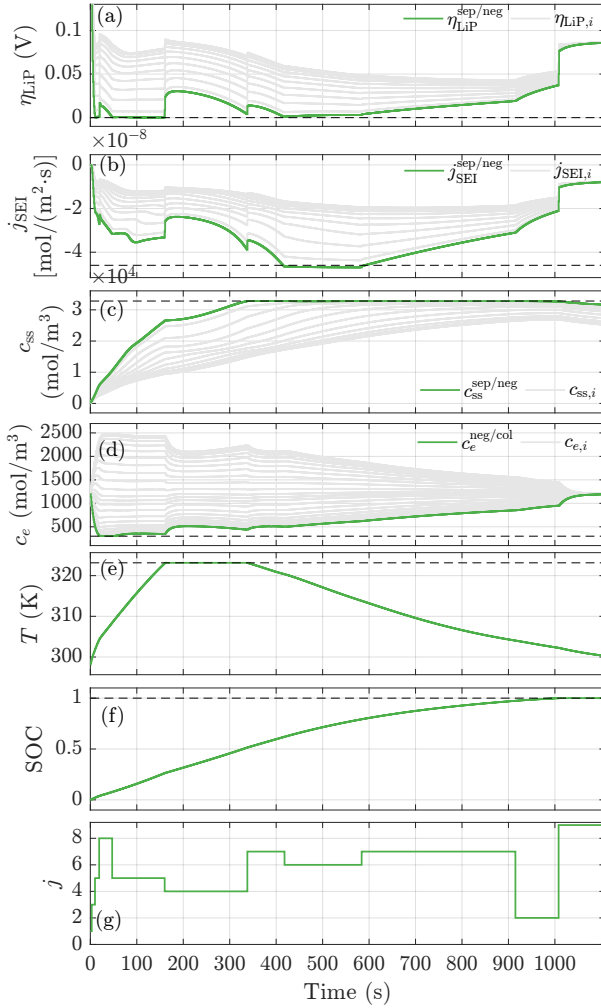
Fig. 4. Outputs when all nine constraints are imposed. (a) Local LiP potentials in the negative electrode. (b) Local SEI side-reaction molar flux. (c) Local solid-phase surface concentrations in the negative electrode. (d) Local electrolyte concentrations. (e) Battery temperature. (f) SOC. (g) Activated control mode. The dashed lines indicate the corresponding bound or tracking reference.

TABLE I
PERFORMANCE COMPARISON OF FAST-CHARGING STRATEGIES

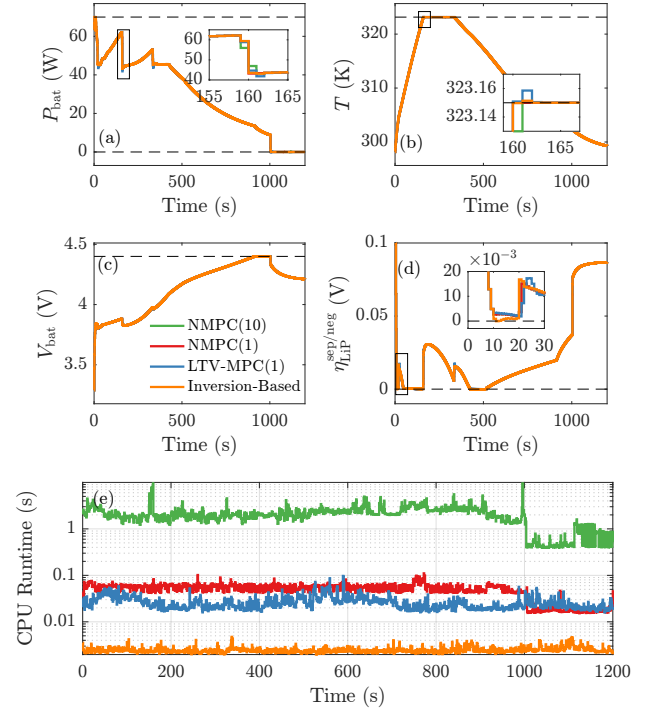| Algorithm	NMPC	NMPC	LTV-MPC	Inv.-Based
Prediction horizon	10	1	1	–
Charging Time	1005 s	1005 s	1005 s	1005 s
RMSE of I_{app}	–	0.003C	0.003C	0.02C
RMSE of SOC	–	0.0001	0.0001	0.0002
MAX of SOC	–	0.0003	0.0003	0.0008
CPU runtime per sample ($\Delta t = 1$ s)	2.32 s	0.0555 s	0.0266 s	0.0024 s

Fig. 5. Comparison of NMPC, LTV-MPC, and the proposed inversion-based control for battery fast charging. The dashed lines represent different bounds. (a) Battery power. (b) Battery temperature. (c) Battery voltage. (d) LiP potential at the sep/neg boundary). (e) CPU runtime per sample time ($\Delta t = 1$ s).

SOC, and the control models based on the profile in Fig. 3(a). In this example, the capability of the charging rate is limited by the current and power ($j = 1, 3$) only at the very beginning of the charging process (i.e., $t \leq 10$ s), while most of the time (10 s $< t \leq 915$ s), it is limited by the internal variables such as temperature, side reactions, and concentrations ($j = 4-8$). At the end of the charging process, the terminal voltage and SOC constraints play the limiting roles ($j = 2, 9$). This result demonstrates the importance of considering the internal electrochemical and thermal behaviors during fast charging, while the conventionally considered factors only have impacts at the very initial and late stages of the charging process. Furthermore, from Figs. 4(a)–(d), we can see the significance of considering the electrode nonuniformity in the electrode when investigating the fast charging of Li-ion batteries.

C. Comparative Studies With NMPC and LTV-MPC

In this subsection, the inversion-based output tracking charging strategy (Alg. 1) is compared with MPC-based schemes. LTV-MPC and NMPC algorithms [38] are used to design three charging strategies based on the same battery model and constraints as in Section II: NMPC with a longer prediction horizon of 10 steps, one-step NMPC, and one-step LTV-MPC. Fig. 5 shows the battery power, temperature, voltage, LiP potential, and CPU runtime using the four strategies, and Table I compares their numerical performances. It shows that one-step NMPC, one-step LTV-MPC, and inversion-based control have achieved the same charging time and very close current/SOC profiles to the NMPC solution with a long prediction horizon. However, the computational cost of the proposed strategy is much lower than the MPCs: It is over 10 and 20 times faster than the one-step LTV-MPC and one-step NMPC strategies, respectively. Furthermore, the inversion-based control can achieve nearly the same results as the NMPC in view of its small root-mean-square error (RMSE) and the maximum absolute error (MAX).
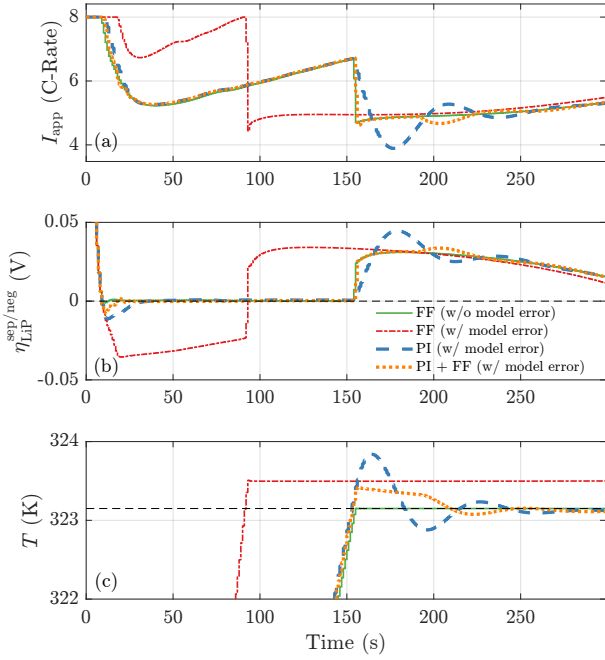
Fig. 6. Effects of model error on control performances with different control schemes. (a) Applied battery current rate. (b) LiP potential ($i = N^{\mathrm{sep/neg}}$). (c) Battery temperature.
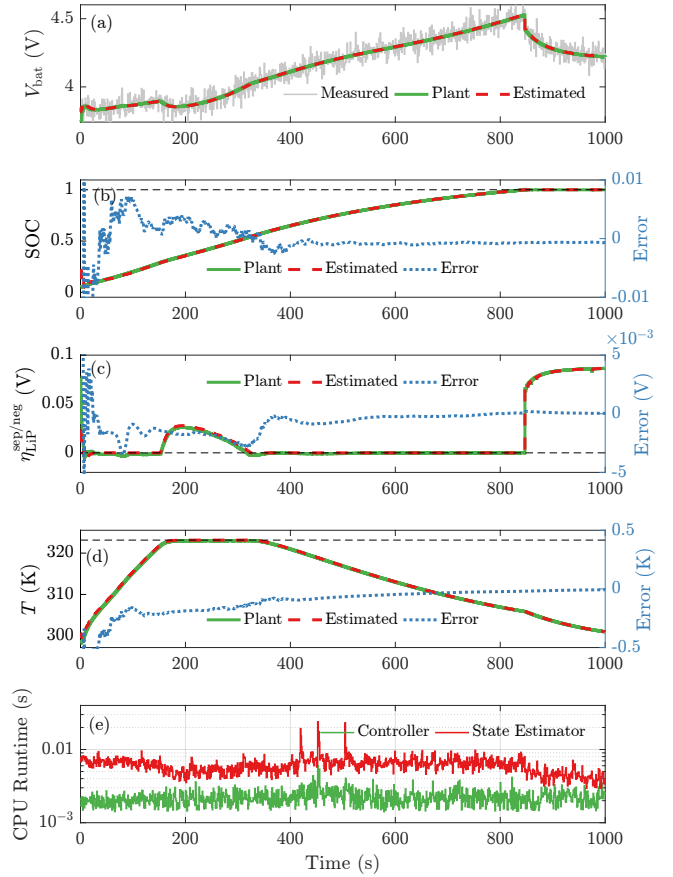

Fig. 7. Performance of the model-inversion-based fast charging control with a state estimator. (a) Voltage. (b) SOC. (c) Lithium plating potential. (d) Battery internal temperature. (e) CPU runtime of the controller and the state estimator.

D. Comparative Studies With PI-Based Feedback Control

As mentioned earlier, the inversion-based control is a model-based FF control and it is thus subject to the accuracy of the model parameters. To enhance the robustness of the control, the FF control can be combined with a PI controller. In the case the output y_j is measurable, the robustness of the controller can be directly enhanced. To demonstrate this, we investigate the CC-CT-Cη_{LiP} control as an example, and assume that we have wrong knowledge on two model parameters: the adopted negative electrode reaction constant k^{eff} in (55) is doubled and the thermal resistance C_T in (14) is decreased to 1/3 of its nominal value. These parameters are usually identified by fitting the experimental data, but can change over time due to varying operating conditions and are affected by aging. Note that the internal temperature T and LiP potential $\eta_{\mathrm{LiP}}^{\mathrm{sep/neg}}$ are not measured in existing commercial battery systems, but they can be accessed in experimental settings with an implanted thermocouple [39] and a reference electrode [40], respectively.

From the first 300-s simulation results shown in Figs. 6(a) and (b), it can be seen that if wrong parametric values are used, the pure FF control fails to correctly predict the current to keep LiP potential nonnegative between 10 s to 92 s, and this can trigger lithium plating. Similarly, Figs. 6(a) and (c) show that, although not very significant, a steady-state temperature error exists caused by the model error. These problems can be addressed by using PI feedback control, but the PI control may create unfavorable overshoots during mode transitions even after being fine-tuned. The scheme by integrating the PI with the FF is advantageous over the pure PI scheme in terms of the enhanced transient: The transient in the PI control

can be better dampened with the aid of the FF compensation, and the corresponding overshoots are also lowered. However, it is important to note that the promised improvement is contingent upon the measurability of the controlled variable. In the future, investigations will be directed to explore the quantitative impact of model parameter uncertainty on the performance of the inversion-based charging control.

E. Fast Charging Control With a State Estimator

The impact of state estimation on the performance of the proposed control will be examined in this subsection. For a high-dimensional nonlinear battery model used in this work, the computationally efficient state estimation can be achieved using ensemble-based methods, such as the ensemble Kalman filter (EnKF) [29] and the ensemble transform Kalman filter [27]. Here, we incorporate an EnKF-based state estimator into the proposed inversion-based fast charging controller. The EnKF is a sequential Monte Carlo implementation of the Bayesian filter. Since the EnKF does not require updating the state covariance matrix as in the conventional Kalman filters and the statistics are represented using its low-rank approximation, it is very computationally efficient for high-dimensional systems such as the present PBM of batteries. In the simulation, we set the number of the ensemble member to
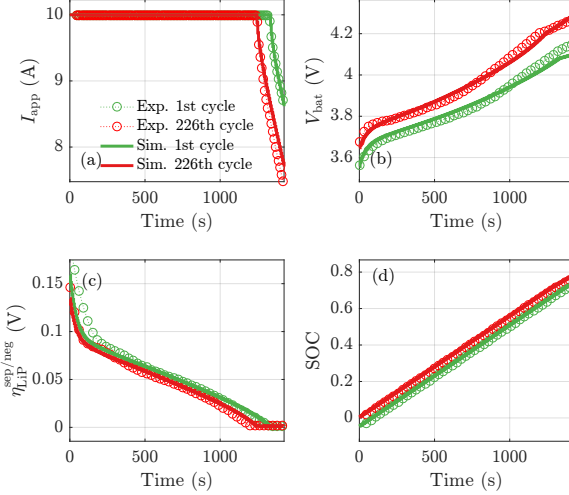
Fig. 8. Comparison of experimental and simulation results based on the CC-Cη_{LiP} strategy. (a) Current rates. (b) Terminal voltage. (c) lithium plating potential. (d) SOC.

5 and introduce a 20% error in the initial guess of SOC and a 2-K error for the temperature to verify the convergency of the inversion-based CC-CT-Cη_{LiP} control. The initial state ensemble was set in a uniform manner as described in [29]. The battery voltage is the single measurement, and the standard deviation of the voltage sensor is assumed to be 20 mV.

The simulation results, including the plant and estimated voltage, SOC, lithium plating potential, internal temperature, estimate errors, and CPU runtime, are shown in Fig. 7. In Fig. 7(a), the noisy voltage measurement is also depicted. It can be observed from Figs. 7(b) and (d) that the estimated SOC and temperature can rapidly converge to the plant value, which is in agreement with the performance of the EnKF as demonstrated in [29]. The SOC estimation error is maintained below 1%, and the internal temperature error is below 0.5 K most of the time. As seen in Fig. 7(b), the lithium plating potential is also accurately estimated with an RMSE of 0.0012 V. However, the results indicate a slight underestimation of the lithium plating potential, necessitating the introduction of a small safety margin in the tracking reference ($\underline{\eta}_{\mathrm{LiP}} > 0$) to prevent triggering of lithium plating.

The computational burden of the state estimator is compared with the controller in Fig. 7(d) in terms of the CPU runtime. It can be seen that although the computation of the EnKF-based state estimator is much higher than the controller, the computational efficiency is still quite high: the average CPU time per sample step considering the controller and the state estimator is about 0.01 s, and this is even lower than the LTV-MPC scheme without considering the state estimator as shown in Table I. Since some recent studies have successfully demonstrated the suitability of similar physics-based battery model-based estimators [41], [42], we will investigate the influence of state estimator's computational efficiency and accuracy on the control performance of the proposed method in the real-time context in our future studies.

F. Experimental Validation

To validate the proposed inversion-based method, a charging/discharging cycling protocol was designed and implemented for a laboratory three-electrode NMC coin cell with a capacity of 5 mA. For demonstration purposes, a simple CC-Cη_{LiP} strategy was used for battery charging then the cell was discharged with constant current. After every 75 cycles, a reference performance test was used for capacity calibration and parameter identification. Initially, the unknown parameters considered to be identified include the concentrations ($c_{s,0\%}^{\mathrm{pos}}$, $c_{s,0\%}^{\mathrm{neg}}$, $c_{s,100\%}^{\mathrm{pos}}$, and $c_{s,100\%}^{\mathrm{neg}}$), solid-phase diffusion coefficients (D_s^{pos} and D_s^{neg}), thermal capacitance C_T, thermal resistance R_T, and SEI film resistance r_f^{neg}. The rest parameters are assumed to be the same as those given in Table A1. In subsequent cycles, only aging-affected parameters, such as SEI film resistance, stoichiometries, and solid-phase diffusion coefficients, are identified. To accomplish this, we employ particle swarm optimization (PSO) as a global optimization technique for parameter identification, where hyperparameters of the optimization algorithm are fine-tuned to improve convergence and optimality.

Since the LiP potential can be measured in this experimental setting with the additional reference electrode, Cη_{LiP} control was achieved by a PI controller without the need to use a model. The reference LiP potential is set to 0.0013 V to consider the effect of additional resistance in the separator and electrode. The measured current, voltage, and LiP potential, as well as the calculated SOC were used as benchmark. Based on the identified parameters, we obtained the corresponding CC-Cη_{LiP} charging current curves and applied them in computer simulation according to the proposed inversion-based approach, and the simulated results of current, voltage, LiP potential, and SOC are compared with the experiment in Fig. 8. The predictive RMSEs of the current and LiP potential are as low as 0.01C and 0.02 V, respectively. It can be seen that using the high-fidelity model, the proposed inversion-based method can accurately predict the benchmark current profile without the measurement of LiP potential, indicating that such a method is well-suited for practical applications where such a measurement of internal variables is not usually available.

VII. CONCLUSIONS

In this paper, we have shown that an internal or an external variable, or their first-order time derivatives, of a PBM, can be expressed in an input-affine or input-quadratic form. This fact motivates us to develop an inversion-based multiple-output tracking strategy for fast charging Li-ion batteries. Different physical operating limits are considered as the tracking references, and the charging current is bounded by complying with the constraint requirement when a given tracking control signal comes into action. Consequently, the charging current is explicitly expressed as a state-dependent function. The input-output control stability and performance are guaranteed by shaping the input-output relationship as a first-order transfer function, and the tuning effort of the control parameters is limited to decide the corresponding time constants. The inversion-based control can function as feedforward compensation to

a PI feedback control to improve the control robustness. The results in the illustrative examples have exhibited the computational superiority of the proposed inversion-based nonlinear control algorithm to LTV-MPC and nonlinear MPC-based control algorithms. The proposed control method can be generalized to a class of battery models if the output variables, or their time derivatives, can be expressed in a low-order input-polynomial form.

APPENDIX

A. Expressions of Circuit Components

The voltage sources and resistances in Fig. 1 are given by

$$U_{\text{ss},i} = U_{\text{ref},i} + \left(\frac{\partial U}{\partial T}\right)_i (T - T_{\text{ref}}) \tag{48}$$

$$U_{e,i} = \frac{2\mathcal{R}Tt_a^0}{\mathcal{F}} \ln\left(\frac{c_{e,i}}{c_e^0}\right) \tag{49}$$

$$R_{e,i+0.5} = \frac{1}{2A}\left(\frac{\Delta\delta_i}{\kappa_i^{\text{eff}}} + \frac{\Delta\delta_{i+1}}{\kappa_{i+1}^{\text{eff}}}\right) \tag{50}$$

$$R_{s,i+0.5} = \frac{1}{2A}\left(\frac{\Delta\delta_i}{\sigma_i^{\text{eff}}} + \frac{\Delta\delta_{i+1}}{\sigma_{i+1}^{\text{eff}}}\right) \tag{51}$$

$$R_e^{\text{sep}} = \sum_{i=N^{\text{pos}}}^{N^{\text{pos}}+N^{\text{sep}}} R_{e,i+0.5} \tag{52}$$

$$R_{\Sigma,i} = R_{\text{ct},i} + R_{f,i} = \frac{r_{\text{ct},i}}{A\Delta\delta_i a_{s,i}} + \frac{r_{f,i}^{\text{eff}}}{A\Delta\delta_i a_{s,i}}, \tag{53}$$

where $U_{\text{ref},i}$ and $\left(\frac{\partial U}{\partial T}\right)_i$ are two nonlinear functions of $c_{\text{ss},i}$ determined by the characteristics of the corresponding electrode (see e.g., Table A1). The voltage sources $U_{\text{ss},i}$ and $U_{e,i}$, and the resistances $R_{e,i+0.5}$, $R_{s,i+0.5}$, and R_e^{sep}, are state-dependent variables. In contrast, resistance $R_{\Sigma,i}$ depends not only on the state but also on the input. This can be seen from the expression of the areal charge-transfer resistance $r_{\text{ct},i}$, given by

$$r_{\text{ct},i} = \frac{\mathcal{R}T}{\mathcal{F}i_{0,i}} \frac{\sinh^{-1}(0.5\mathcal{F}j_{n,i}/i_{0,i})}{0.5\mathcal{F}j_{n,i}/i_{0,i}} \tag{54}$$

where

$$i_{0,i} = \mathcal{F}k_i^{\text{eff}}\sqrt{c_{e,i}c_{\text{ss},i}(c_{s,\max,i} - c_{\text{ss},i})} \tag{55}$$

$$j_{n,i} = I_{n,i}/(\mathcal{F}A\Delta\delta_i a_{s,i}) \tag{56}$$

are the exchange current density and pore-wall molar flux, respectively. The intercalation current $I_{n,i}$ in (56) is a function of state and input, as seen from (1). Since solving $I_{n,i}$ based on the circuit requires all circuit elements to be state-dependent, a gradient-free method is adopted here to iteratively approximate $r_{\text{ct},i}$ and $I_{n,i}$, described as follows.

Step 1: Give all state-dependent circuit components based on the initial system states, input current I_{app}, and an initial guess of $I_{n,i} = I_{\text{app}}/N^{\text{pos}}, \forall i \in \mathcal{I}^{\text{pos}}$ and $I_{n,i} = -I_{\text{app}}/N^{\text{neg}}, \forall i \in \mathcal{I}^{\text{neg}}$.

Step 2: Calculate $r_{\text{ct},i}$ and $R_{\Sigma,i}$ according to (54)–(56).

Step 3: Solve the circuit in Fig. 1 for a new $I_{n,i}$.

Repeat Step 2 and Step 3 until $I_{n,i}$ has converged.

B. State-Dependent Coefficients of the Heat Generation

R_Q, V_Q, and Q_Q are three state-dependent coefficients in the units of resistance, voltage, and power (heat transfer rate), respectively. The expressions of the coefficients are

$$R_Q = R_{Q,\text{rev}} + R_{Q,\text{rxn}} + R_{Q,\text{ohm}}$$
$$V_Q = V_{Q,\text{rev}} + V_{Q,\text{rxn}} + V_{Q,\text{ohm}}$$
$$Q_Q = Q_{Q,\text{rev}} + Q_{Q,\text{rxn}} + Q_{Q,\text{ohm}}$$

where

$$R_{Q,\text{rxn}} = \sum_{i\in\mathcal{I}^{\text{pos}}\cup\mathcal{I}^{\text{neg}}} (K_{n,i}^{\text{ZSR}})^2 R_{\Sigma,i}$$

$$V_{Q,\text{rxn}} = \sum_{i\in\mathcal{I}^{\text{pos}}\cup\mathcal{I}^{\text{neg}}} 2K_{n,i}^{\text{ZSR}} I_{n,i}^{\text{ZIR}} R_{\Sigma,i}$$

$$Q_{Q,\text{rxn}} = \sum_{i\in\mathcal{I}^{\text{pos}}\cup\mathcal{I}^{\text{neg}}} (I_{n,i}^{\text{ZIR}})^2 R_{\Sigma,i}$$

$$R_{Q,\text{rev}} = 0$$

$$V_{Q,\text{rev}} = \sum_{i\in\mathcal{I}^{\text{pos}}\cup\mathcal{I}^{\text{neg}}} K_{n,i}^{\text{ZSR}} T\left(\frac{\partial U}{\partial T}\right)_i$$

$$Q_{Q,\text{rev}} = \sum_{i\in\mathcal{I}^{\text{pos}}\cup\mathcal{I}^{\text{neg}}} I_{n,i}^{\text{ZIR}} T\left(\frac{\partial U}{\partial T}\right)_i$$

$$R_{Q,\text{ohm}} = R_{\text{col}} + R_e^{\text{sep}} + \sum_{i\in\mathcal{I}'} (K_{e,i+0.5}^{\text{ZSR}})^2 R_{e,i+0.5}$$

$$V_{Q,\text{ohm}} = \sum_{i\in\mathcal{I}'} 2K_{e,i+0.5}^{\text{ZSR}} I_{e,i+0.5}^{\text{ZIR}} R_{e,i+0.5}$$
$$+ \sum_{i=1}^{N^{\text{tot}}-1} K_{e,i+0.5}^{\text{ZSR}} (U_{e,i+1} - U_{e,i})$$

$$Q_{Q,\text{ohm}} = \sum_{i\in\mathcal{I}'} (I_{e,i+0.5}^{\text{ZIR}})^2 R_{e,i+0.5}$$
$$+ \sum_{i=1}^{N^{\text{tot}}-1} I_{e,i+0.5}^{\text{ZIR}} (U_{e,i+1} - U_{e,i})$$

C. Model Parameters

The fidelity of the P2D-T model has been verified in many existing works (see, e.g., [27]) and the procedure will thus not be repeated in the present investigation. Instead, the model parameters are obtained from the software GT AutoLion for a 2.4-Ah NMC-Graphite cell as given in Table A1.

REFERENCES

[1] Department of Energy, USA. (2022, 17 Jan.) Model year 2021 all-electric vehicles had a median driving range about 60% that of gasoline powered vehicles. [Online]. Available: https://www.energy.gov/eere/vehicles/articles/fotw-1221-january-17-2022-model-year-2021-all-electric-vehicles-had-median

[2] P. H. L. Notten, J. H. G. Op het Veld, and J. R. G. van Beek, "Boostcharging Li-ion batteries: A challenging new charging concept," *J. Power Sources*, vol. 145, no. 1, pp. 89–94, Jul. 2005.

[3] Y. Liu and Y. Luo, "Search for an optimal rapid-charging pattern for Li-ion batteries using the Taguchi approach," *IEEE Trans. Ind. Electron.*, vol. 57, no. 12, pp. 3963–3971, Dec. 2010.

[4] L. Chen, S. Wu, D. Shieh, and T. Chen, "Sinusoidal-ripple-current charging strategy and optimal charging frequency study for Li-ion batteries," *IEEE Trans. Ind. Electron.*, vol. 60, no. 1, pp. 88–97, Jan. 2013.

TABLE A1
ELECTROCHEMICAL PARAMETERS OF LI-ION BATTERY MODEL

$\mathcal{D}$ $i \in \mathcal{I}^{\mathcal{D}}$	pos $\mathcal{I}^{\text{pos}}$	sep $\mathcal{I}^{\text{sep}}$	neg $\mathcal{I}^{\text{neg}}$
$\delta^{\mathcal{D}}$	75.8×10^{-6}	20×10^{-6}	82.5×10^{-6}
$\Delta\delta_i$	$\delta^{\text{pos}}/N^{\text{pos}}$	$\delta^{\text{sep}}/N^{\text{sep}}$	$\delta^{\text{neg}}/N^{\text{pos}}$
$R_{p,i}$	10×10^{-6}	–	10×10^{-6}
$c_{s,\max,i}$	$49,500$	–	$33,491$
$c_{s,0\%}^{\mathcal{D}}$	$45,478$	–	321
$c_{s,100\%}^{\mathcal{D}}$	$16,330$	–	$39,724$
$\varepsilon_{s,i}$	0.68	–	0.69
$a_{s,i}$	$203,040$	–	$205,860$
k_i	2.4×10^{-11}	–	3.7×10^{-11}
$D_{s,i}$	3.0×10^{-14}	–	1.6×10^{-14}
σ_i	3.8	–	100
$r_{f,i}$	0	–	0.01
$E_{a,i}^{k}$	$50,000$	–	$68,000$
$E_{a,i}^{D_s}$	$30,000$	–	$30,000$
$E_{a,i}^{\sigma}$	$20,000$	–	$20,000$
$E_{a,i}^{r_f}$	$20,000$	–	$20,000$
$\varepsilon_{e,i}$	0.28	0.4	0.27
c_e^0	1200		
t_a^0	0.62		
T_{ref}	298.15		
A	0.0593		
C_T	17.79		
R_T	8.43		

1) The expressions of $D_{e,i}^{\text{eff}}$ and κ_i^{eff} as functions of electrolyte concentration and temperature are obtained from [23].

2) For parameters $\phi \in \{k, D_s, \sigma, r_f\}$, the Arrhenius equation holds.

$$\phi_i^{\text{eff}} = \phi_i \exp\left(-\frac{E_{a,i}^{\phi}}{\mathcal{R}}\left(\frac{1}{T} - \frac{1}{T_{\text{ref}}}\right)\right)$$

3) OCP of an NMC electrode ($i \in \mathcal{I}^{\text{pos}}, \theta := c_{\text{ss},i}/c_{s,\max,i}$):
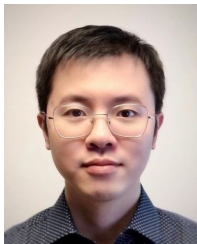
$$U_{\text{ref},i} = -1282.47\theta^7 + 5638.32\theta^6 - 10441.91\theta^5 + 10534.02\theta^4$$
$$- 6237.84\theta^3 + 2.166.06\theta^2 - 410.2481\theta + 37.1596$$

4) OCP of a graphite electrode ($i \in \mathcal{I}^{\text{neg}}, \theta := c_{\text{ss},i}/c_{s,\max,i}$):

$$\begin{aligned}U_{\text{ref},i} =& 0.1397 + 0.8493\exp\left(-61.79\theta\right) + \\ & 0.3824\exp\left(-665.8\theta\right) - \exp\left(39.42\theta - 41.92\right) - \\ & 0.03131\tan^{-1}(25.59\theta - 4.099) - \\ & 0.009434\tan^{-1}(32.49\theta - 15.74)\end{aligned}$$

optimization for lithium-ion batteries," *J. Power Sources*, vol. 313, pp. 164–177, May 2016.

[13] J. Liu, G. Li, and H. K. Fathy, "An extended differential flatness approach for the health-conscious nonlinear model predictive control of lithium-ion batteries," *IEEE Trans. Control Syst. Technol.*, vol. 25, no. 5, pp. 1882–1889, Sep. 2017.

[14] R. Klein, N. A. Chaturvedi, J. Christensen, J. Ahmed, R. Findeisen, and A. Kojic, "Optimal charging strategies in lithium-ion battery," in *Proc. Amer. Control Conf.*, 29 Jun.-1 Jul. 2011, pp. 382–387.

[15] M. Xu, R. Wang, P. Zhao, and X. Wang, "Fast charging optimization for lithium-ion batteries based on dynamic programming algorithm and electrochemical-thermal-capacity fade coupled model," *J. Power Sources*, vol. 438, p. 227015, Oct. 2019.

[16] C. Zou, X. Hu, Z. Wei, T. Wik, and B. Egardt, "Electrochemical estimation and control for lithium-ion battery health-aware fast charging," *IEEE Trans. Ind. Electron.*, vol. 65, no. 8, pp. 6635–6645, Aug. 2018.

[17] A. Goldar, R. Romagnoli, L. D. Couto, M. Nicotra, M. Kinnaert, and E. Garone, "Low-complexity fast charging strategies based on explicit reference governors for Li-ion battery cells," *IEEE Trans. Control Syst. Technol.*, vol. 29, no. 4, pp. 1597–1608, Jul. 2021.

[18] L. D. Couto, R. Romagnoli, S. Park, D. Zhang, S. J. Moura, M. Kinnaert, and E. Garone, "Faster and healthier charging of lithium-ion batteries via constrained feedback control," *IEEE Trans. Control Syst. Technol.*, vol. 30, no. 5, pp. 1990–2001, 2022.

[19] F. Lam, A. Allam, W. T. Joe, Y. Choi, and S. Onori, "Offline multiobjective optimization for fast charging and reduced degradation in lithium-ion battery cells using electrochemical dynamics," *IEEE Control Syst. Lett.*, vol. 5, no. 6, pp. 2066–2071, 2021.

[20] X.-G. Yang and C.-Y. Wang, "Understanding the trilemma of fast charging, energy density and cycle life of lithium-ion batteries," *J. Power Sources*, vol. 402, pp. 489–498, Oct. 2018.

[21] A. M. Boyce, D. J. Cumming, C. Huang, S. P. Zankowski, P. S. Grant, D. J. L. Brett, and P. R. Shearing, "Design of scalable, next-generation thick electrodes: Opportunities and challenges," *ACS Nano*, vol. 15, no. 12, pp. 18 624–18 632, Dec. 2021.

[22] M. A. Xavier, A. K. d. Souza, K. Karami, G. L. Plett, and M. S. Trimboli, "A computational framework for lithium ion cell-level model predictive control using a physics-based reduced-order model," *IEEE Control Syst. Lett.*, vol. 5, no. 4, pp. 1387–1392, Oct. 2021.

[23] Y. Li, M. Vilathgamuwa, T. Farrell, S. S. Choi, N. T. Tran, and J. Teague, "A physics-based distributed-parameter equivalent circuit model for lithium-ion batteries," *Electrochim. Acta*, vol. 299, pp. 451–469, Mar. 2019, doi: 10.1016/j.electacta.2018.12.167.

[24] B. Suthar, P. W. C. Northrop, R. D. Braatz, and V. R. Subramanian, "Optimal charging profiles with minimal intercalation-induced stresses for lithium-ion batteries using reformulated pseudo 2-dimensional models," *J. Electrochem. Soc.*, vol. 161, no. 11, pp. F3144–F3155, Oct. 2014.

[25] S. Kolluri, S. V. Aduru, M. Pathak, R. D. Braatz, and V. R. Subramanian, "Real-time nonlinear model predictive control (NMPC) strategies using physics-based models for advanced lithium-ion battery management system (BMS)," *J. Electrochem. Soc.*, vol. 167, no. 6, p. 063505, Apr. 2020.

[26] A. Pozzi, M. Zambelli, A. Ferrara, and D. M. Raimondo, "Balancing-aware charging strategy for series-connected lithium-ion cells: A nonlinear model predictive control approach," *IEEE Trans. Control Syst. Technol.*, vol. 28, no. 5, pp. 1862–1877, Sep. 2020.

[27] Y. Li, D. M. Vilathgamuwa, E. Wikner, Z. Wei, X. Zhang, T. Thiringer, T. Wik, and C. Zou, "Electrochemical model-based fast charging: Physical constraint-triggered PI control," *IEEE Trans. Energy Convers.*, vol. 36, no. 4, pp. 3208–3220, Dec. 2021, doi: 10.1109/TEC.2021.3065983.

[28] N. T. Tran, M. Vilathgamuwa, T. Farrell, S. S. Choi, and Y. Li, "A computationally efficient coupled electrochemical-thermal model for large format cylindrical lithium ion batteries," *J. Electrochem. Soc.*, vol. 166, no. 13, pp. A3059–A3071, Sep. 2019.

[29] Y. Li, B. Xiong, D. M. Vilathgamuwa, Z. Wei, C. Xie, and C. Zou, "Constrained ensemble Kalman filter for distributed electrochemical state estimation of lithium-ion batteries," *IEEE Trans. Ind. Informat.*, vol. 17, no. 1, pp. 240–250, Jan. 2021, doi: 10.1109/TII.2020.2974907.

[30] N. A. Chaturvedi, R. Klein, J. Christensen, J. Ahmed, and A. Kojic, "Algorithms for advanced battery-management systems," *IEEE Control Syst. Mag.*, vol. 30, no. 3, pp. 49–68, Jun. 2010.

[31] C. Zou, C. Manzie, and D. Nesic, "A framework for simplification of PDE-based lithium-ion battery models," *IEEE Trans. Control Syst. Technol.*, vol. 24, no. 5, pp. 1594–1609, Sep. 2016.

[32] Y. Li, T. Wik, C. Xie, Y. Huang, B. Xiong, J. Tang, and C. Zou, "Control-oriented modeling of all-solid-state batteries using physics-

[5] A. Tomaszewska *et al.*, "Lithium-ion battery fast charging: A review," *eTransport.*, vol. 1, p. 100011, Aug. 2019.

[6] Y. Lee and S. Park, "Electrochemical state-based sinusoidal ripple current charging control," *IEEE Trans. Power Electron.*, vol. 30, no. 8, pp. 4232–4243, Aug. 2015.

[7] S. Wang and Y. Liu, "A PSO-based fuzzy-controlled searching for the optimal charge pattern of Li-ion batteries," *IEEE Trans. Ind. Electron.*, vol. 62, no. 5, pp. 2983–2993, May 2015.

[8] C. Zou, X. Hu, Z. Wei, and X. Tang, "Electrothermal dynamics-conscious lithium-ion battery cell-level charging management via state-monitored predictive control," *Energy*, vol. 141, pp. 250–259, Dec. 2017.

[9] Y. Li, D. Karunathilake, D. M. Vilathgamuwa, Y. Mishra, T. W. Farrell, S. S. Choi, and C. Zou, "Model order reduction techniques for physics-based lithium-ion battery management: A survey," *IEEE Ind. Electron. Mag.*, vol. 16, no. 3, pp. 36–51, Sep. 2022, doi: 10.1109/MIE.2021.3100318.

[10] Z. Wei, Z. Quan, J. Wu, Y. Li, J. Pou, and H. Zhong, "Deep deterministic policy gradient-drl enabled multiphysics-constrained fast charging of lithium-ion battery," *IEEE Trans. Ind. Electron.*, vol. 69, no. 3, pp. 2588–2598, Mar. 2022.

[11] B. Jiang, M. D. Berliner, K. Lai, P. A. Asinger, H. Zhao, P. K. Herring, M. Z. Bazant, and R. D. Braatz, "Fast charging design for lithium-ion batteries via bayesian optimization," *Appl. Energy*, vol. 307, p. 118244, Feb. 2022.

[12] S. Pramanik and S. Anwar, "Electrochemical model based charge

based equivalent circuits," *IEEE Trans. Transport. Electrific.*, vol. 8, no. 2, pp. 2080–2092, Aug. 2022, doi: 10.1109/TTE.2021.3131147.

[33] M. Luo, M.-T. F. Rodrigues, L. L. Shaw, and D. P. Abraham, "Examining effects of negative to positive capacity ratio in three-electrode lithium-ion cells with layered oxide cathode and Si anode," *ACS Appl. Energy Mat.*, vol. 5, no. 5, pp. 5513–5518, 2022.

[34] S. Park, D. Lee, H. J. Ahn, C. Tomlin, and S. Moura, "Optimal control of battery fast charging based-on Pontryagin's minimum principle," in *IEEE Conf. Decis. Control*, 14-18 Dec. 2020, pp. 3506–3513.

[35] S. Devasia, D. Chen, and B. Paden, "Nonlinear inversion-based output tracking," *IEEE Trans. Autom. Control*, vol. 41, no. 7, pp. 930–942, Jul. 1996.

[36] E. Moulay and W. Perruquetti, "Stabilization of nonaffine systems: A constructive method for polynomial systems," *IEEE Trans. Autom. Control*, vol. 50, no. 4, pp. 520–526, Apr. 2005.

[37] S. Devasia, "Should model-based inverse inputs be used as feedforward under plant uncertainty?" *IEEE Trans. Autom. Control*, vol. 47, no. 11, pp. 1865–1871, Nov. 2002.

[38] S. Gros, M. Zanon, R. Quirynen, A. Bemporad, and M. Diehl, "From linear to nonlinear MPC: Bridging the gap via the real-time iteration," *Int. J. Control*, vol. 93, no. 1, pp. 62–80, Jan. 2020.

[39] D. Anthony, D. Wong, D. Wetz, and A. Jain, "Non-invasive measurement of internal temperature of a cylindrical Li-ion cell during high-rate discharge," *Int. J. Heat Mass Transfer*, vol. 111, pp. 223–231, 2017.

[40] M.-T. F. Rodrigues, K. Kalaga, S. E. Trask, D. W. Dees, I. A. Shkrob, and D. P. Abraham, "Fast charging of Li-ion cells: Part I. using Li/Cu reference electrodes to probe individual electrode potentials," *J. Electrochem. Soc.*, vol. 166, no. 6, pp. A996–A1003, 2019.

[41] J. Sturm, S. Ludwig, J. Zwirner, C. Ramirez-Garcia, B. Heinrich, M. F. Horsche, and A. Jossen, "Suitability of physicochemical models for embedded systems regarding a nickel-rich, silicon-graphite lithium-ion battery," *J. Power Sources*, vol. 436, p. 226834, Oct. 2019.

[42] F. F. Oehler, K. Nrnberger, J. Sturm, and A. Jossen, "Embedded real-time state observer implementation for lithium-ion cells using an electrochemical model and extended Kalman filter," *J. Power Sources*, vol. 525, p. 231018, Mar. 2022.

Torsten Wik received the M.Sc. degree in chemical engineering (major in applied mathematics), the Licentiate of Engineering degree in control engineering, the Ph.D. degree in environmental sciences (major in automatic control), and the Docent degree in electrical engineering from the Chalmers University of Technology, Gothenburg, Sweden, in 1994, 1996, 1999, and 2004, respectively. From 2005 to 2007, he was a Senior Researcher with Volvo Technology, Gothenburg, researching on control system design for combustion engine test cells, and combined reformer and fuel cells. He is a Professor and the Head of the Automatic Control Group, Department of Electrical Engineering, Chalmers University of Technology.

His current research interests include optimal control, model reduction, and systems with model uncertainties, with applications to energy storage, environmental, and biological systems.
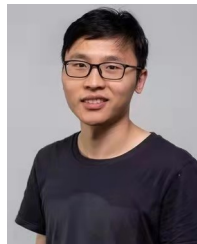
Yicun Huang received the M.Eng. degree from the University of Bristol, UK, in 2015, and the Ph.D. degree from the School of Engineering, University of Canterbury, Christchurch, New Zealand, in 2020, both in mechanical engineering. He is currently a Postdoctoral Researcher with the Department of Electrical Engineering, Chalmers University of Technology, Gothenburg, Sweden. His research interests include advanced modeling for energy materials.

Dr. Huang is a recipient of the 2022 Marie Skłodowska-Curie Postdoctoral Fellow and the Best Presentation Award of the 2022 International Conference on Energy and AI.

Yang Li (Senior Member, IEEE) received the B.E. degree in electrical engineering from Wuhan University, Wuhan, China, in 2007, and the M.Sc. and Ph.D. degrees in power engineering from Nanyang Technological University (NTU), Singapore, in 2008 and 2015, respectively.

He was a Research Fellow with the Energy Research Institute, NTU and the School of Electrical Engineering and Computer Science, Queensland University of Technology, Brisbane, QLD, Australia. He joined the School of Automation, Wuhan University of Technology, Wuhan, in 2019, as a faculty member. Since 2020, he has been a Researcher with the Department of Electrical Engineering, Chalmers University of Technology, Gothenburg, Sweden. His research interests include modeling and control of energy storage systems in power grid and transport sectors. Dr. Li serves as an Associate Editor for several journals such as IEEE TRANSACTIONS ON INDUSTRIAL ELECTRONICS, IEEE TRANSACTIONS ON TRANSPORTATION ELECTRIFICATION, and IEEE TRANSACTIONS ON ENERGY CONVERSION.

Changfu Zou (Senior Member, IEEE) received the Ph.D. degree in automation and control engineering from the University of Melbourne, Melbourne, VIC, Australia, in 2017.

He was a Visiting Student Researcher at the University of California, Berkeley, Berkeley, CA, USA, from 2015 to 2016. Since early 2017, he has been with the Automatic Control unit, Chalmers University of Technology, Gothenburg, Sweden, where he started as a Post-Doctoral Researcher and then became an Assistant Professor and is currently an Associate Professor. His research focuses on advanced modeling and automatic control of energy storage systems, particularly batteries.

Dr. Zou has been awarded several prestigious grants from the European Commission and Swedish national agencies and has hosted four researchers to achieve the Marie Skłodowska-Curie Fellows. He serves as an Associate Editor/Editorial Board Member for journals, such as IEEE TRANSACTIONS ON VEHICULAR TECHNOLOGY, IEEE TRANSACTIONS ON TRANSPORTATION ELECTRIFICATION, and Cell Press journal iScience.